Regional uncertainty of GOSAT XCO_2 retrievals in China: Quantification and attribution

Nian Bie[1, 2], Liping Lei[1], ZhaoCheng Zeng[3], Bofeng Cai[4], Shaoyuan Yang[1, 2], Zhonghua He[1, 2], Changjiang Wu[1, 2], and Ray Nassar[5]

[1]Key Laboratory of Digital Earth Science, Institute of Remote Sensing and Digital Earth, Chinese Academy of Sciences, Beijing 100094, China

[2]University of Chinese Academy of Sciences, Beijing 100049, China

[3]Division of Geological and Planetary Sciences, California Institute of Technology, Pasadena, CA91125, USA

[4]The Center for Climate Change and Environmental Policy, Chinese Academy for Environmental Planning, Ministry of Environmental Protection, Beijing, 100012, China

[5]Climate Research Division, Environment and Climate Change Canada, Canada

Correspondence to: leilp@radi.ac.cn

Abstract. The regional uncertainty of XCO_2 (column-averaged dry air mole fraction of CO_2) retrieved using different algorithms from the Greenhouse gases Observing SATellite (GOSAT) and its attribution are still not well understood. This paper investigates the regional performance of XCO_2 within a latitude band of 37°N~ 42°N segmented into 8 cells in a grid of 5° from west to east (80°E ~120°E) in China, where there are typical land surface types and geographic conditions. The former include the various land covers of desert, grassland and built-up areas mixed with cropland, and the latter include anthropogenic emissions that change from small to large from west to east, including those from the megacity of Beijing. For these specific cells, we evaluate the regional uncertainty of GOSAT XCO_2 retrievals by quantifying and attributing the consistency of XCO_2 retrievals from four algorithms (ACOS, NIES, OCFP, and SRFP) by intercomparison. Particularly, these retrievals are compared with simulated XCO_2 by the high-resolution nested model in East Asia of Goddard Earth Observing System 3-D chemical transport model (GEOS-Chem). We introduce the anthropogenic CO_2 emissions data generated from the investigation of surface emitting point sources that was conducted by the Ministry of Environmental Protection of China to GEOS-Chem simulations of XCO_2 over the Chinese mainland. The results indicate that (1) regionally, the four algorithms demonstrate smaller absolute biases of 0.7-1.1 ppm in eastern cells, which are covered by built-up areas mixed with cropland with intensive anthropogenic emissions, than those in the western desert cells (1.0-1.6 ppm) with a high-brightness surface from the pairwise comparison results of XCO_2 retrievals. The inconsistency of XCO_2 from the four algorithms tends to be high in the Taklimakan Desert in western cells, which is likely induced by high surface albedo in addition to dust aerosols in this region. (2) Compared with XCO_2 simulated by GEOS-Chem (GEOS-XCO_2), the XCO_2 values of ACOS and SRFP have better agreement with GEOS-XCO_2, while OCFP is the least consistent with GEOS-XCO_2. (3) Viewing attributions of XCO_2 in the spatio-temporal pattern, ACOS and SRFP demonstrate similar patterns, while OCFP is largely different from the others. In conclusion, the discrepancy in the four algorithms is the smallest in eastern cells in the study area, where the megacity of Beijing is located and where there are strong anthropogenic CO_2 emissions, which implies

that XCO_2 from satellite observations could be reliably applied in the assessment of atmospheric CO_2 enhancements induced by anthropogenic CO_2 emissions. The large inconsistency among the four algorithms presented in western deserts with a high albedo and dust aerosols, moreover, demonstrates that further improvement is still necessary in such regions, even though many algorithms have endeavored to minimize the effects of aerosols scattering and surface albedo.

Key words: GOSAT, XCO_2 retrieval algorithms, simulated XCO_2 by GEOS-Chem, regional uncertainty, anthropogenic emissions, and desert

1 Introduction

The column-averaged dry air mole fraction of CO_2 (XCO_2) derived from satellite observations, such as the SCanning Imaging Absorption spectroMeter of Atmospheric CHartographY (SCIAMACHY) (Burrows et al., 1995; Bovensmann et al., 1999) , the Greenhouse gases Observing SATellite (GOSAT) (Yokoda et al., 2004), Orbiting Carbon Observatory (OCO-2) (Crisp et al., 2004), have greatly improved our understanding of the variation in atmospheric CO_2 concentration and carbon sources and sinks at a global and regional scale. There have been several full-physics retrieval algorithms specially developed for retrieving XCO_2 from the GOSAT observed spectrum, mainly including the NASA Atmospheric CO_2 Observations from Space (ACOS) (O'Dell et al., 2012), the National Institute for Environmental Studies (NIES) (Yoshida et al., 2013), the University of Leicester full-physics XCO_2 (OCFP) (Cogan et al., 2012) and the RemoTeC XCO_2 Full Physics (SRFP) (Butz et al., 2011).

Retrieval of XCO_2 from space is susceptible to the effects of light path changes due to aerosol scattering, uncertainties in observed spectrum and surface states (O'Dell et al., 2012; Oshchepkov et al., 2013). The bias and performance of XCO_2 retrievals from an algorithm could change in different regions with differing land surfaces and anthropogenic emissions. Spatio-pattern attributions of XCO_2 viewed from different algorithms are also different, even in the same region, due to different physical approaches adopted by the algorithms, assumptions of atmospheric conditions (aerosol, surface pressure, CO_2 profile, etc.), and pre- and post-processing filters. Currently, the validation of XCO_2 retrievals from different algorithms focuses on using ground-based measurements from Total Carbon Column Observing Network (TCCON) sites (Wunch et al., 2011; Yoshida et al., 2013; Hewson, 2016; Buchwitz et al., 2015, Detmers et al., 2015, Oshchepkov et al., 2013) and their consistency evaluation and cross-comparison both at a global scale and in continental regions (Kulawik et al., 2016; Lindqvist et al., 2015; Lei et al., 2014).The precision and uncertainty of satellite-retrieved XCO_2 outside TCCON stations, most of which are located remote from regions with abundant biosphere fluxes and human activities, are still not well evaluated. The sparseness of TCCON stations over the globe, moreover, means a lack of enough ground observations to validate satellite retrievals. Specifically, there are no good TCCON data available in China, and only a few satellite retrievals have been validated using ground-based Fourier Transform Spectrometer (FTS) XCO_2 measurements in Hefei (Wang et al., 2017). In the analysis and application of XCO_2 data from ACOS, NIES, OCFP and SRFP, we found that unreasonably high

XCO_2 was presented in the Taklimakan desert in China (Bie et al., 2016; Liu et al., 2015). For this reason, we extended the study scope to select a longer study period and to further assess the overall performance of these four algorithms at a regional scale.

With the advantage of continuity in space and time, atmospheric transport model simulation of CO_2 has been widely used in assessing the performance of satellite-retrieved XCO_2 (Cogan et al., 2012; Lindqvist et al., 2015; Kulawik et al., 2016). As anthropogenic emission of CO_2 is the major contributor to increases of CO_2 in the atmosphere, many studies have been involved in deriving estimates of anthropogenic CO_2 emissions (Oda et al., 2011; Andres et al., 2011). It is known that there exists high uncertainty in estimates of CO_2 emissions from both the burning of fossil fuel and cement production (FF CO_2 emissions) throughout China (Guan et al., 2012; Liu et al., 2015). As noted by Andrews et al. (2012), there exist many kinds of restrictions (e.g., commercial competitiveness reasons) in obtaining accurate data on sub-national (e.g., large-point-source or provincial) FF CO_2 emissions. Furthermore, the assumption of uniform per-capita emissions within a country has also been shown to be unreliable for large countries with diversified economies and electricity-generation methods (Nassar et al., 2013). In the previous study of Keppel-Aleks (2013), the simulated Chinese XCO_2 data was increased by a national uniform ratio for the corresponding XCO_2 contributed by fossil sources to account for the underestimation in Chinese emissions, in which way the spatial variability of Chinese FF emissions was not considered sufficient.

In this paper, we focus on a latitude band of 37°N-42°N from 80°E to 120°E in China, where there are various typical land covers such as desert, including the Taklimakan desert, and grassland and built-up areas mixed with croplands, including the megacity of Beijing, and there are anthropogenic emissions increasing from west to east. In this band, the inconsistencies of XCO_2 values derived from four algorithms including ACOS V3.5, NIES V02.21, OCFP V6.0 and SRFP V2.3.7 are compared and evaluated in this paper. A forward model simulation data set from GEOS-Chem, moreover, is also used for intercomparison. To improve the simulation of CO_2 concentration by GEOS-Chem, we introduced a new emission data set, the Chinese High Resolution Emission Gridded Data (CHRED) which is produced by the Ministry of Environmental Protection, China (MEP) based on investigations of emitting point sources from approximately 150 million enterprises throughout the country in 2012 (Wang et al., 2014; Cai et al., 2014).

First, we aim to reveal the regional uncertainty of XCO_2 observed by GOSAT for the different land covers and anthropogenic CO_2 emission regions by quantifying the inconsistency of the four retrieval algorithms. Second, we aim to provide a reasonable and valuable reference for the analysis and application of XCO_2 data when using these XCO_2 data from the four algorithms. Sec. 2 in this paper describes the XCO_2 retrievals data from four algorithms and the implementation of XCO_2 simulated by GEOS-Chem using CHRED. Inconsistencies of XCO_2 datasets among the four algorithms are quantified and evaluated by (1) pairwise comparisons of XCO_2 between algorithms and (2) comparisons with GEOS-Chem simulations in Sec. 3. The spatio-temporal patterns of XCO_2 from each algorithm are investigated using a combination of sine and cosine trigonometric functions to fit monthly averaged XCO_2 from March 2010 to February 2013 in Sec. 4. Furthermore, the most likely attribution-affecting factors on regional inconsistency, including aerosol and surface albedo, are discussed in Sec. 5. The latest ACOS V7.3 dataset, moreover, is also used by cross-comparisons with GEOS-Chem and other algorithms

including ACOS V3.5, NIES V02.21, OCFP V6.0 and SRFP V2.3.7, as shown in subsections of Sec. 5. Finally, the regional performances of four algorithms and the regional uncertainty of GOSAT XCO2 retrievals from the results described above are summarized, and conclusions are given in Sec. 6.

2 Study area and data

2.1 Study area

The latitude band of 37°N~42°N from 80°E to 120°E in China is selected as the study area, which is segmented into eight cells in a grid of 5°x5° units for comparison and evaluation. The study area has two typical surface characteristics as shown in Fig. 1, supporting our assessment of the performance of XCO_2 retrievals from four algorithms: (1) the amounts of anthropogenic CO_2 emissions from west to east significantly varies from small to large as shown in Fig. 1(a). The emission data are from the Open-source Data Inventory for Anthropogenic CO_2 (ODIAC), a global annual fossil fuel CO_2 emission inventory developed by combining a worldwide point-source database and satellite observations of the global nightlight distribution (Oda et al., 2011). There are almost no anthropogenic CO_2 emissions in the western cells ending at 105°E, while there is high anthropogenic emission located in the cells on the eastern end of the latitude band. (2) There are typical land covers from west to east, as shown in Fig. 1 (b), mainly composed of desert (desert sand in the two cells from 80°E to 90°E, Gobi in the two cells from 90°E to 100°E, desert sand in the cell of 100°E-105°E), grassland in the cell of 105°E-110°E, and cropland and built-up areas in the two cells from 110°E to 120°E. These characteristics are associated with complicated aerosol compositions and loadings. One of the main reasons for focusing on this latitude band, moreover, is because there are more high-quality GOSAT scans available in this area compared to other areas in China.

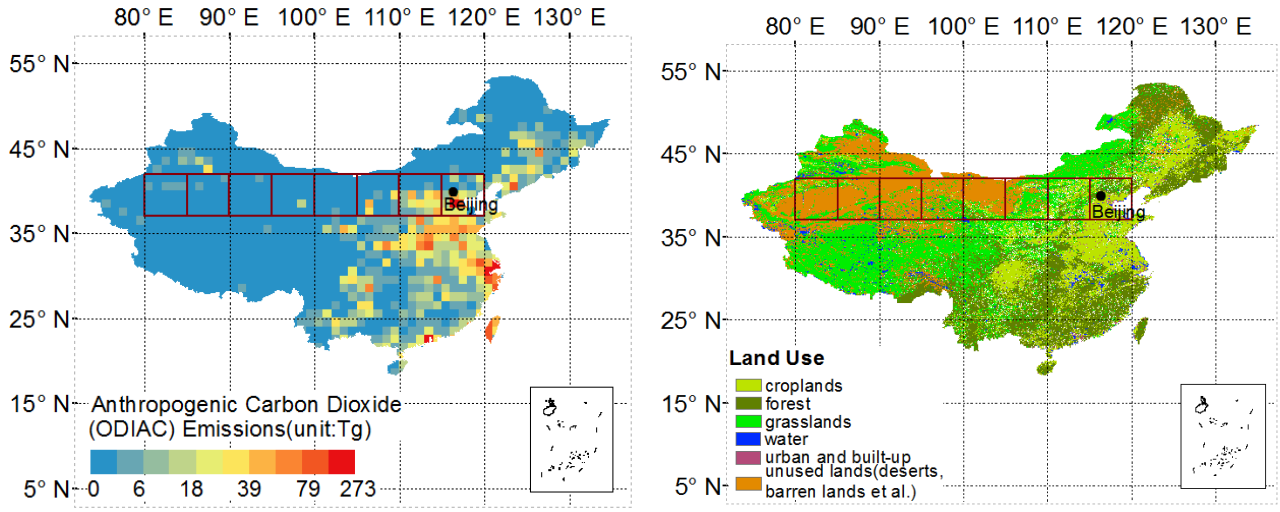

Fig. 1. (a)Location of the study area segmented into cells (deep red cells) in China and annual fossil fuel CO_2 emission in 2012 (1 x 1 degree) from ODIAC and (b) land use mapping in 2010, where the black dot represents Beijing, the capital of China.

2.2 GOSAT XCO_2 dataset derived from four algorithms

We collected XCO_2 data from March 2010 to February 2013 derived from four algorithms: ACOS V3.5 (http://CO_2.jpl.nasa.gov), NIES V02.21 (RA version with GU screening scheme) (https://data2.gosat.nies.go.jp), OCFP V6.0 (http://www.esa-ghg-cci.org) and SRFP V2.3.7 (http://www.esa-ghg-cci.org). AOD and surface albedo in 0.75-um O_2 band, which are necessary for our further analysis, are also collected from attached datasets in each algorithms except that albedo is not available for OCFP. The major characteristics of the four algorithms and the relevant references are listed in Table 1. The validation at TCCON sites for all algorithms indicates that the bias is less than 1.2 ppm on average and that the standard deviation is less than 2.0 ppm. All algorithms take aerosol optical depth (AOD) into consideration in their data screening scheme but in slightly different ways. The collected XCO_2 data from ACOS, OCFP and SRFP are the products after bias correction. Data observed with high gain and passing the corresponding recommended quality control criteria are used in ACOS, NIES, OCFP and SRFP.

Table 1 Summary of validating results with TCCON, data screening schemes, consideration in scattering and bias corrections for the four retrieval algorithms.

	ACOS	NIES	OCFP	SRFP
Validation with TCCON[*1]	0.3 ppm 1.7 ppm	-1.2 ppm 2.0 ppm	0.04 ppm 1.78 ppm	0.01 ppm 1.93 ppm
Data screening schemes	Aerosol_total_aod: 0.015 to 0.25 Sounding_altitude:<3000 0.55<XCO_2_uncer<2.0 ppm Aod_dust<0.15 The difference of the retrieved and priori surface pressure from the A-band cloud-screen Δ Ps,cld : (-12,4.1) hPa	Retrieved aerosol optical thickness: <=0.1 Difference of retrieved and a priori surface pressure: <=20 hpa Blended albedo: <1	Retrieved type 1 (small) AOD: <=0.3 Retrieved type 2 (large) AOD: <=0.15 Retrieved ice type AOD: <=0.025 Error on retrieved XCO_2 :<=2.15	Aerosol optical thickness : <0.3 3<aero_size<5 0<aerosol_filter<300 Error on retrieved XCO_2: <1.2 ppm standard deviation of surface elevation within GOSAT ground pixel: <80 m Blended albedo: <0.9
Consideration in scattering	4 extinction profiles (two aerosol types , water and ice cloud)	logarithms of the mass mixing ratios of fine-mode aerosols and coarse mode aerosols with aerosol optical properties based on SPRINTARS V3.84	Aerosol profile scaling of 2 different aerosol types; cloud extinction profile scaling	Aerosol particle number concentration, aerosol size parameter, aerosol height
Bias corrections	$X'_{CO_2} = X_{CO_2} - 0.5 - 0.155*\left(\Delta P_{s,cld} + 2.7\right) + 10.6*\left(\alpha'_3 - 0.204\right) + 0.0146*\left(\Delta GRAD_{CO_2} - 35\right) + 12.8*(AOD_{DUST} - 0.01)$ See details in the product user guide.	-	Via a regression analysis of the difference between GOSAT and TCCON XCO_2 land observations. See details in the product user guide	$X'_{CO_2} = X_{CO_2} *(1.002837 + 2.1176e-5*\phi)$ ϕ : the aerosol filter
References	GES DISC, 2016; O'Dell et al., 2012; D.Wunch et al., 2011.	NIES (GOSAT Project Office), 2015; Yoshida et al., 2013; D.Wunch et al., 2011.	Hew, 2016; GHG-CCI group at University of Leicester, 2014.	Detmers et al., 2015; Hasekamp et al., 2015

[*1]The first represents mean biases, and the second represents overall standard deviations.

Within the study area, the total numbers of valid GOSAT XCO_2 observations are 3345, 3556, 2282 and 3685 for ACOS, NIES, OCFP and SRFP, respectively. Figure 2 shows the number of available XCO_2 retrievals for 4 seasons (spring: MAM; summer: JJA; autumn: SON; winter: DJF). It can be seen that the number of available XCO_2 retrievals is clearly smaller in spring and summer than that in autumn and winter due to different meteorological conditions and data-screening processes.

The cloudiness in spring and summer caused by the monsoon climate disturbs satellite observation, while the smaller data number in the west of 110 °E is due to frequent dust storm in the Taklimakan Desert.

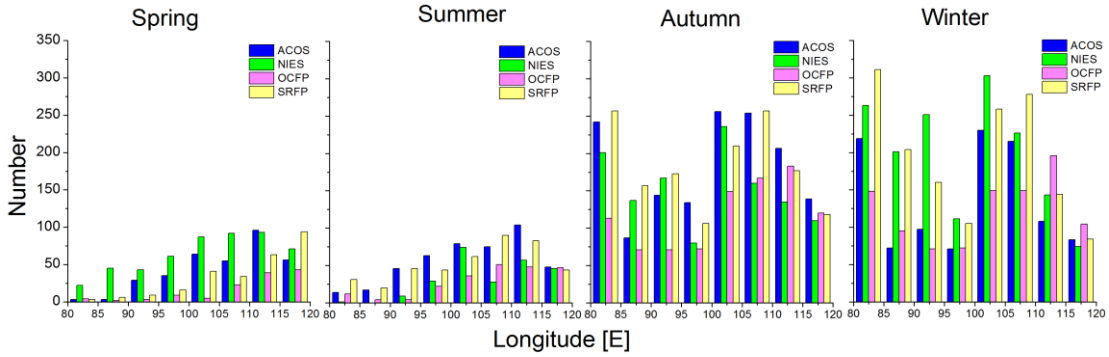

Fig. 2. Number of single scans from the four GOSAT-XCO_2 data sets from ACOS, NIES, OCFP and SRFP over each 5x5 ° cells for different seasons (Spring: MAM; summer: JJA; autumn: SON; winter: DJF) from March 2010 to February 2013.

2.3 XCO_2 simulations from GEOS-Chem

We use GEOS-Chem version 10-01 driven by GEOS-5 and the details of the main input emissions are as follows: 1) Fossil fuel fluxes are taken from the new emission data set CHRED for the Chinese mainland, we also use ODIAC version 2013 for comparison with CHRED. 2) The balanced biosphere CO2 uptake and emission fluxes are taken from the Simple Biosphere Model version 3 (SiB3) [Messerschmidt et al. 2012]. 3) Biomass emissions are taken from Global Fire Emission Database version 4 (GFEDv4) (Giglio et al., 2013). 4) Ocean fluxes are taken as Takahashi et al. (2009) suggested. A detailed description of these input emissions for the GEOS-Chem CO_2 simulation is pesented in Nassar et al. (2010), although we have used some of the most recent updates available in the GEOS-Chem version 10-01 and the Harvard–NASA Emission Component version 1.0 (HEMCO) module (Keller et al., 2014), a versatile component for emissions in atmospheric models. Higher model resolution is critical in the calculation of the concentrations of atmospheric gases, especially over land where topography smoothing (compared to reality) is determined by horizontal resolution (Ciais et al., 2010). Considering this, GEOS-Chem nested grid model in China at 0.5 ° (latitude) x 0.666 ° (longitude) horizontal resolution, is used for the CO_2 simulation with boundary conditions provided by the global model at 2 ° (latitude) x 2.5 ° (longitude) resolution. We made a restart file with 386.4 ppm for both the global simulation and the nested simulation on 1 January 2009 based on NOAA ESRL data. Both the global model and the nested-grid model were run twice, driven by the same CO_2 fluxes from January 2009 to February 2013 except that the ODIAC was chosen for the first run and CHRED for the second as the input fossil-fuel fluxes over the Chinese mainland. Model CO_2 profiles (averages for local hours between 12:00 pm and 13:30 pm) were presented from January 2010 to February 2013, allowing sufficient time for the high-resolution model to adjust to transients introduced by the initialization of the model on 1 January 2009. The pressure-weighting function described in Connor (2008) was applied to convert level-based modeling CO_2 to XCO_2.

Fig.3 presents the spatial difference of emissions over the Chinese mainland between CHRED and ODIAC at a horizontal resolution of 1 °x1 °. The values of emissions from CHRED are mostly larger than those from ODIAC, as shown in Fig. 3, and this difference tends to be large in the eastern part of our study area. In addition, the difference in their total emissions, 10.38 Pg CO_2 for CHRED versus 9.64 Pg CO_2 for ODIAC, is not small. ODIAC is also found to exhibit an overestimation of emissions in large cities compared to CHRED.

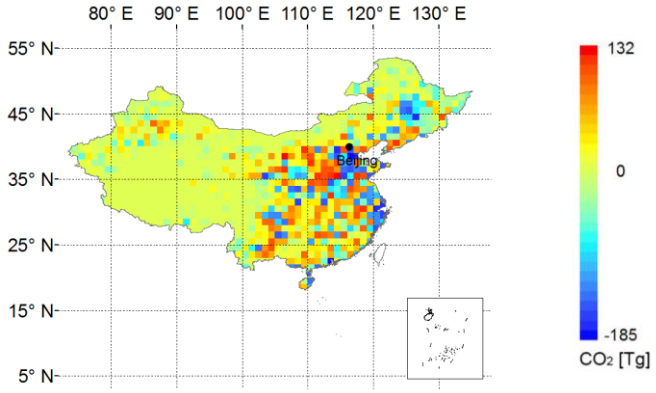

Fig. 3. Difference of annual total anthropogenic CO_2 emissions between CHRED and ODIAC in 2012 in China, where the black dot represents Beijing, the capital of China.

For each 1 °x1 °grid, the corresponding annual CO_2 emissions in the years from 2009 to 2012 were allocated by the ratio of emissions in CHRED to that in ODIAC in 2012. We acquired the new input inventory of CO_2 emissions, CHRED, by scaling the obtained yearly emissions with the ratio of monthly emissions to the yearly ones in ODIAC. In this way, we altered the spatial and temporal distribution, but not at temporal scales finer than monthly. This is expected to be an improvement upon the current ODIAC emission values.

The annually averaged XCO_2 simulations, driven separately by CHRED and ODIAC respectively, are calculated and shown in Fig. 4. The impact of emission deviations of CHRED from ODIAC is significant, with XCO_2 from CHRED larger by 0.7 ppm on average over China. There are also obvious differences in spatial patterns, especially in Northwest China, Northeast China, North China and South China. XCO_2 simulations from CHRED are larger by more than 0.7 ppm in most parts east of 100 °E with a maximum of 1.4 ppm compared to those from ODIAC. The increase in the annual mean, which should not be ignored, is approximately 1.0 ppm for east of 110 °E in the study latitude band. The CO_2 profile dataset from CHRED are used to compare with satellite-retrieved XCO_2 in our following experiments.

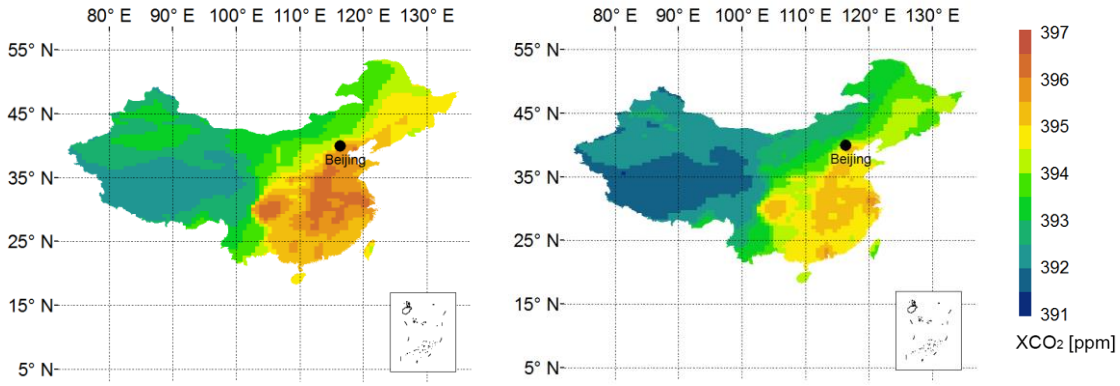

Fig. 4. Annual mean of XCO_2 simulations driven by CHRED (left) and ODIAC (right) in 2012 in China, where the black dot represents Beijing, the capital of China.

We compared GEOS-Chem CO_2 simulations from the global model driven by CHRED with daily mean TCCON data from 14 TCCON sites (version GGG2014 data version) (Blumenstock et al., 2014; Deutscher et al., 2014; Griffith et al., 2014a, 2014b; Hase et al., 2014; Kawakami et al., 2014; Kivi et al., 2014; Morino et al., 2014; Sherlock et al., 2014; Sussmann et al., 2014; Warneke et al., 2014; Wennberg et al., 2014a, 2014b, 2014c). All TCCON measurements between 12 pm and 13:30 pm are used in the comparisons, where GEOS-Chem CO_2 profiles are taken according to the location of TCCON stations (latitude and longitude) as well as the observing date and transformed to XCO_2 by convolved with the individual averaging kernel in each station as Wunch (2010) suggested. The statistics results are shown in Table 2.

Table 2. Statistics of comparison between GEOS-Chem CO_2 simulations driven by CHRED and TCCON data from January 2010 to February 2013, which includes biases (Δ), the standard deviations (δ), the correlation coefficients (r) and valid days (days) when TCCON data are available. Δ, δ and r are calculated using coincident daily mean data averaged between 12:00 pm and 13:30 pm.

ID	Station name	Latitude	Longitude	Δ[ppm]	δ[ppm]	r	days
1	Sodankyla	67.37	26.63	2.03	2.00	0.83	269
2	Bialystok	53.23	23.02	0.49	1.84	0.87	196
3	Karlsruhe	49.1	8.44	0.84	1.69	0.84	152
4	Orleans	47.97	2.11	0.44	1.70	0.85	223
5	Garmisch	47.48	11.06	0.65	1.64	0.83	293
6	Park Falls	45.94	-90.27	1.17	2.14	0.75	494
7	Lamont	36.6	-97.49	-0.04	1.22	0.90	642
8	Tsukuba	36.05	140.12	1.43	1.66	0.75	217
9	JPL	34.2	-118.18	-1.30	1.15	0.90	289
10	Saga	33.24	130.29	-0.39	1.65	0.86	159
11	Izana	28.3	-16.48	0.85	1.04	0.90	114
12	Darwin	-12.43	130.89	0.65	0.90	0.88	447
13	Wollongong	-34.41	150.88	0.53	0.83	0.94	347
14	Lauder	-45.04	169.68	0.92	0.42	0.97	370
	Mean			0.59±0.80	1.42±0.50		

The results of Table 2 show that the bias ranges from -1.30 to 2.03 ppm for all TCCON sites with standard deviations of the difference varying from 0.42 to 2.14 ppm. The mean standard deviation at the TCCON sites, a measure of the achieved overall precision, from using GEOS-Chem simulations driven by CHRED is 1.42±0.50 ppm which is slightly different from using GEOS-Chem simulations driven by ODIAC (1.41±0.49 ppm). Those validated results with TCCON comparing GEOS-Chem CO_2 simulations driven by CHRED to that by ODIAC indicate that the GEOS-Chem CO_2 simulations driven by CHRED is more likely not to change the global magnitude of CO_2 concentration but rather to depict fine spatial distribution of CO_2 concentration in China.

2.4 Aerosol optical depth and surface albedo data

The monthly mean aerosol optical depth (A0D) data were collected from the NASA Earth Observing System's Multi-angle Imaging Spectro-radiometer (MISR) Level 3 Component Global Aerosol Product, downloaded from the website https://eosweb.larc.nasa.gov/project/misr. The released GLASS (Glass Land Surface Satellites) albedo product GLASS02B06 (http://glcf.umd.edu/data/abd/) is used, which is a gapless, long-term continuous and self-consistent data-set with accuracy similar to that of the Moderate Resolution Imaging Spectrometer (MODIS) MCD43 product (Liu et al., 2013). GLASS02B06 is a daily land-surface shortwave (300-3000nm) broadband albedo product in temporal resolution of eight days.

3 Quantification of agreement of XCO_2 retrievals from four algorithms in the footprints

We focus on the difference of each footprint XCO_2 retrieval in this section. Comparison of XCO_2 from four algorithms with GEOS-Chem CO_2 simulations driven by CHRED, and pairwise comparisons of XCO_2 between algorithms were calculated as a quantified indicator of their differences.

3.1 Comparisons with GEOS-Chem CO_2 simulations

We used the nested GEOS-Chem CO_2 simulations driven by CHRED as a baseline to quantify the regional consistency of the four algorithms. The collocated model CO_2 profile is averaged over the local hours of 12:00-13:30 pm corresponding to the local time of overpass and locations (latitude and longitude) of GOSAT. To compare XCO_2 retrievals from ACOS, NIES, OCFP and SRFP, corresponding GEOS-XCO_2 data were created by applying averaging kernels from each algorithm to model CO_2 profiles as suggested by Rodgers (2003). Correlation diagrams of XCO_2 between GEOS-Chem (X) and GOSAT (Y) for the four algorithms are shown in Fig. 5. The regression slope (a), the coefficient of determination (R^2), the correlation coefficient (r), and biases of GOSAT (Y) from GEOS-Chem(X) are also shown in the inset of each panel.

It can be seen from Fig. 5 that the linear fits and the correlations with GEOS-Chem are better for ACOS and OCFP (R^2 approximately 0.66) than for either NIES or SRFP (R^2 approximately 0.59). The regression slope is the closest to unity in the OCFP panel (0.94) and is lightly less than OCFP in the ACOS panel (0.87), which means the best similarity in variation. The

slope is less than 0.8 in the NIES and SRFP panels. The bias of GEOS-Chem vs ACOS and SRFP is less than 0.5 ppm while it is 2 ppm and 1.2 ppm vs NIES and OCFP, respectively.

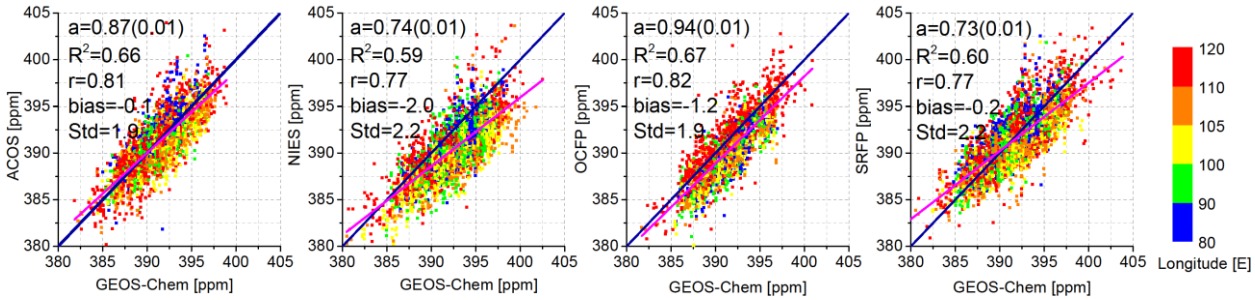

Fig. 5: Correlation diagrams of GOSAT XCO_2 (Y) for the four algorithms vs GEOS-XCO_2 (X). Statistics from linear regression fit are also shown. GEOS-Chem data are selected according to the locations and time of XCO_2 retrievals from the four algorithms in cells. Deep blue solid lines represent 1:1 lines, and the magenta lines demonstrate the best linear regression fit for all samples. Colored points represent XCO_2 for different longitude cells in the study latitude band [37 °N, 42 °N] shown in Fig.1, where colors for each cell are indicated in the right legend.

Table 3 shows the biases and number of samples used between each algorithm and GEOS-Chem in each cell. It can be seen that the biases of ACOS and SRFP vs GEOS-Chem in all cells are below 1 ppm, which implies better consistency with GEOS-Chem regionally than NIES and OCFP. NIES presents 1.2-3.1 ppm lower than GEOS-Chem in all cells excluding the cell of 115 °E, which is likely due to no corrections of the existing systematic biases in the NIES data set (Yoshida et al., 2013). The bias of OCFP vs GEOS-Chem is larger than 1.2 ppm toward the west of 110 °E, while it is 0.1 ppm toward the east of 110 °E. The standard deviations of all the four algorithms with GEOS-Chem range from 1.4 ppm to 2.5 ppm in all cells.

Table 3. The biases (ppm) and their standard deviations (ppm) of the four algorithms vs GEOS-Chem in each cell, where the upper line indicates bias (the corresponding standard deviations in parenthesis) for each algorithm vs GEOS-Chem and the lower line is the available number of used samples. The biases, larger than 1 ppm, are highlighted in bold and underlined.

Left longitude of cells(°E)	80	85	90	95	100	105	110	115
ACOS	0.7(1.6) 478	0.5(1.6) 179	-0.4(1.4) 316	-0.3(1.5) 303	-0.7(1.7) 629	-0.7(1.7) 599	0.0(2.2) 515	0.5(2.1) 326
NIES	**-1.4**(1.7) 487	**-1.6**(1.8) 383	**-1.6**(1.8) 470	**-2.3**(2.5) 281	**-3.0**(1.9) 700	**-3.1**(2.2) 506	**-1.6**(2.5) 428	-0.7(2.4) 301
OCFP	**-1.8**(1.4) 277	**-1.8**(1.5) 172	**-2.2**(1.4) 149	**-1.2**(2.0) 175	**-2.3**(1.6) 339	**-1.5**(1.6) 390	-0.1(1.9) 466	-0.1(2.1) 314
SRFP	0.1(1.9) 602	0.0(1.8) 387	0.2(1.7) 388	-0.2(2.0) 271	**-1.2**(1.9) 571	-0.6(2.7) 659	0.2(2.4) 467	0.0(2.4) 340

3.2 Pairwise comparisons of XCO_2 between algorithms

We made comparisons of geometrically and timely matching pairs XCO_2 between algorithms in each cell. The pairs of XCO_2 retrievals were matched between two algorithms timely in the same day and geometrically located within ±0.01° in latitude and longitude. Figure 6 shows pairwise comparisons of XCO_2 retrievals between two algorithms that demonstrate

the regression slope (a), the coefficient of determination (R^2), the correlation coefficient (r), the number of matching pairs (n) and the biases between every pair of algorithms.

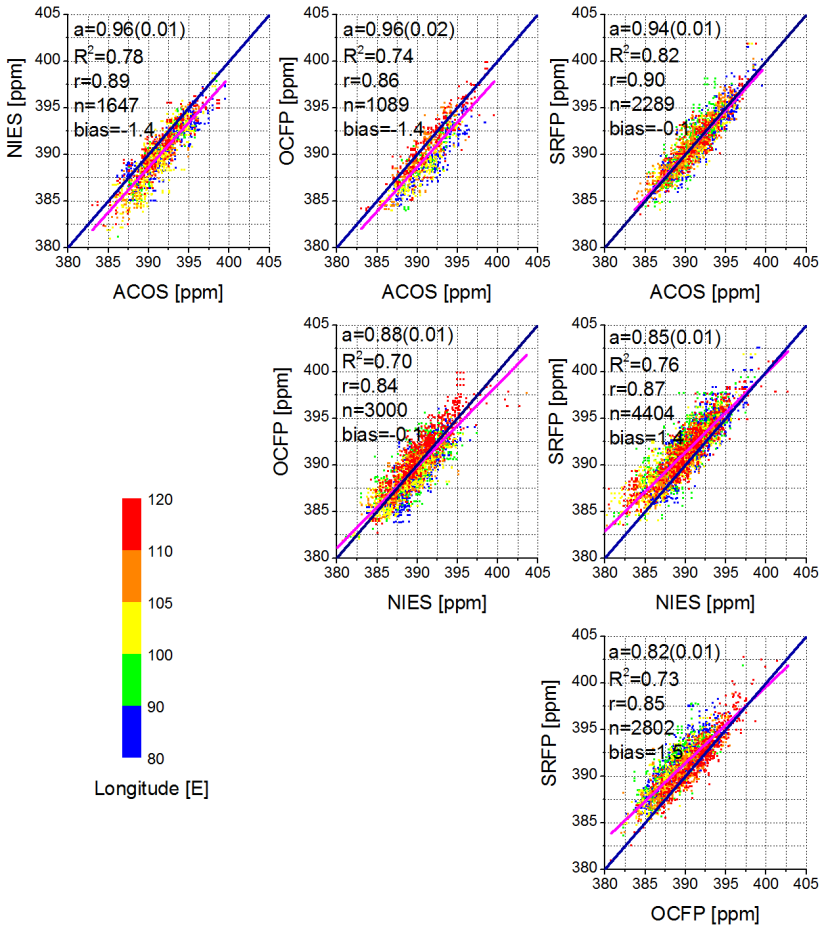

Fig. 6: Algorithm correlation diagrams and statistical characteristics (insets of panels). GOSAT-Y observations were selected over land within ±0.01 ° latitude/longitude of each GOSAT-X observation and in the same day. Deep blue solid lines represent 1:1 lines, and the magenta ones display the best linear regression fit for all observations. Colored points represent XCO_2 for different cells: blue-[80 °E, 90 °E], green-[90 °E, 100 °E], yellow-[100 °E, 105 °E], orange-[105 °E, 110 °E], and red-[110 °E, 120 °E] in the study latitude zone [37 °N, 42 °N].

It can be seen from Fig. 6 that ACOS generally demonstrates the best agreement with other algorithms (top panel). OCFP generally presents biases larger than 1.4 ppm with other algorithms except for 0.1 ppm compared to NIES. It can also be seen from the colored points in Fig. 6 that matching pairs of XCO_2 for OCFP vs ACOS and SRFP mostly concentrated along the 1:1 line in the eastern cells of 105-120 °E (orange and red points) but drifted from the 1:1 line in the western cells of 80-100 °E (blue and green points).

The differences(biases) of matching pairs (the number ranging from 11 to 945) of XCO_2 between two algorithms, moreover, were calculated for each cell as shown in Table 4, and the totally averaged absolute differences of matching pairs of XCO_2 for an algorithm with the other algorithms were also calculated in each cell as shown in Table 5.

It can be found from Table 4 that the difference is mostly less than 1 ppm in those eastern cells with a longitude greater than 105°E, and their consistency can be seen in Fig. 6 (red points between 110-120°E) as well. The differences that are larger than 2 ppm are located in western cells with longitudes less than 105°E, and these differences are mostly shown in OCFP vs other algorithms. The total differences shown in Table 5, moreover, indicate that the differences of the four algorithms tend to be similar to the results of matching pairs of XCO_2 (Table 4), and NIES presents the largest difference up to 1.6 ppm in the western cells of 95°E.

Table 4. Differences (ppm) between two algorithms (column algorithm minus row algorithm) and the corresponding standard deviation (ppm) for each cell, where values in parentheses are the corresponding standard deviations. The differences, larger than 1.5 ppm, are highlighted in bold and underlined.

	*	NIES	OCFP	SRFP	*	NIES	OCFP	SRFP
ACOS	80 °E	-1.4(1.2)	**-2.6**(1.2)	-0.5(1.2)	100 °E	**-1.6**(1.6)	**-2.0**(1.1)	-0.2(1.2)
NIES			-0.9(1.4)	1.1(1.4)			-0.4(1.4)	1.4(1.5)
OCFP				**2.0**(1.2)				**1.7**(1.3)
ACOS	85 °E	**-2.0**(1.3)	**-1.9**(1.2)	-0.1(1.2)	105 °E	**-1.6**(1.3)	-0.6(1.4)	0.2(1.2)
NIES			-0.4(1.6)	1.5(1.3)			0.2(1.5)	1.2(1.3)
OCFP				**2.3**(1.4)				1.0(1.3)
ACOS	90 °E	-1.2(1.1)	**-1.7**(1.1)	0.8(1.4)	110 °E	-1.2(1.3)	-0.9(1.4)	0.0(1.4)
NIES			-0.8(1.4)	**2.0**(1.4)			0.7(1.3)	1.5(1.6)
OCFP				**2.4**(1.5)				0.5(1.2)
ACOS	95 °E	**-3.0**(1.1)	-0.9(1.7)	-0.3(1.2)	115 °E	-0.6(1.3)	0.1(1.0)	-0.1(1.0)
NIES			0.5(2.1)	1.3(2.0)			0.8(1.5)	0.9(1.3)
OCFP				**1.8**(1.6)				0.2(1.3)

The columns labeled with * represent the left longitude of cells (°E).

Table 5. The average of the absolute differences (ppm) and standard deviation (ppm) of the target algorithm (in column) matching all other algorithms for each cell. Values in parentheses are the corresponding standard deviations. The differences, which are larger than 1.5 ppm, are highlighted in bold and underlined.

Left longitude of cells(°E)	80	85	90	95	100	105	110	115
ACOS	1.3(1.1)	1.2(1.0)	1.0(0.7)	1.4(1.2)	1.2(0.9)	1.0(0.7)	0.9(0.6)	0.7(0.5)
NIES	1.1(0.7)	1.3(0.9)	1.2(0.9)	**1.6**(1.2)	1.1(0.8)	1.1(0.8)	1.1(0.8)	0.9(0.6)
OCFP	**1.5**(1.1)	1.4(1.0)	1.4(1.0)	1.3(0.9)	1.2(0.9)	0.9(0.6)	0.8(0.6)	0.8(0.6)
SRFP	1.1(0.9)	1.2(1.0)	1.4(1.1)	1.2(0.9)	1.1(0.8)	0.9(0.6)	1.0(0.7)	0.8(0.5)

To summarize the quantification and analysis in this section, XCO_2 retrievals from two algorithms, ACOS and SRFP are mostly consistent, and the bias of ACOS from GEOS-Chem is the least among the four algorithms. The difference of XCO_2 from cross-comparing four algorithms tends to be less in cells east of 100°E than that in the cells west of 100°E.

4 Comparison of the spatio-temporal pattern revealed by XCO_2 from the four algorithms and simulation

We used a combination of sine and cosine trigonometric functions to statistically fit the seasonal variation of XCO_2, which was originally proposed by Keeling et al. (1976) and has been applied extensively in many studies (Thoning et al. 1989; Kulawik et al., 2016; Lindqvist et al., 2015; Zeng et al., 2016; He et al., 2017). Better attributions are thus obtained for XCO_2 variation in the seasonal cycle and in spatial background patterns by filtering the noise and filling gaps in the original XCO_2 data.

Firstly, the monthly averaged XCO_2 was calculated in each cell using XCO_2 retrievals; then the fit function (Keeling, 1976), expressed as the following equation [1], was applied to the monthly averaged XCO_2 from March, 2010 to February, 2013 for the four algorithms and GEOS-Chem.

$$\mathrm{X}(\mathrm{t}) = A_1 \sin 2\pi t + A_2 \cos 2\pi t + A_3 \sin 4\pi t + A_4 \cos 4\pi t + A_5 + A_6 t \qquad [1]$$

where t represents elapsed time in years, A_1-A_4 are the coefficients determining the seasonal cycle, A_5 represents the initial state of XCO_2 with seasonal variation removed, which can be regarded as the corresponding background concentration, and A_6 is the slope of the linear part in the yearly increase ignoring the minor non-linear part. To derive A_1-A_6 with the above formula, least squares were applied to fit the input monthly weighted means with the corresponding standard deviations as measures of errors. The monthly weighted means (e.g., X (t)) and the corresponding standard deviations in each cell were calculated with the weights inversely proportional to the square of retrieval uncertainty in each observation point.

The accuracy of fitting X(t) depends on the number of gaps in the available XCO_2 retrievals in time and in space resulting from the filtering mechanism for quality controlling. We introduce the Pearson's correlation, hereafter referred to as R, between the input and the predicted results from equation [1] and the unit weighted mean square error, hereafter referred to as σ, in fitting as an uncertainty to judge whether the fitting results are reasonable or not. In addition, we applied equation [1] to the GEOS-Chem dataset, which has been converted to XCO_2 as Connor (2008) suggested. Since atmospheric transport models do not share the same error sources with satellite retrieval algorithms and produces continuous simulations without data gaps, GEOS-Chem provides helpful a priori information for reference.

4.1 Seasonal variation of XCO_2 retrievals

The time series in each cell are acquired for each algorithm using the above formula [1]. The monthly fitted XCO_2 from March 2010 to February 2013 in each cell for the four algorithms as well as GEOS-Chem is shown in Fig. 7. The seasonal amplitudes (the difference between seasonal cycle maximums and minimums) and uncertainty of the fitting function as described by R and σ above are demonstrated in Table 6.

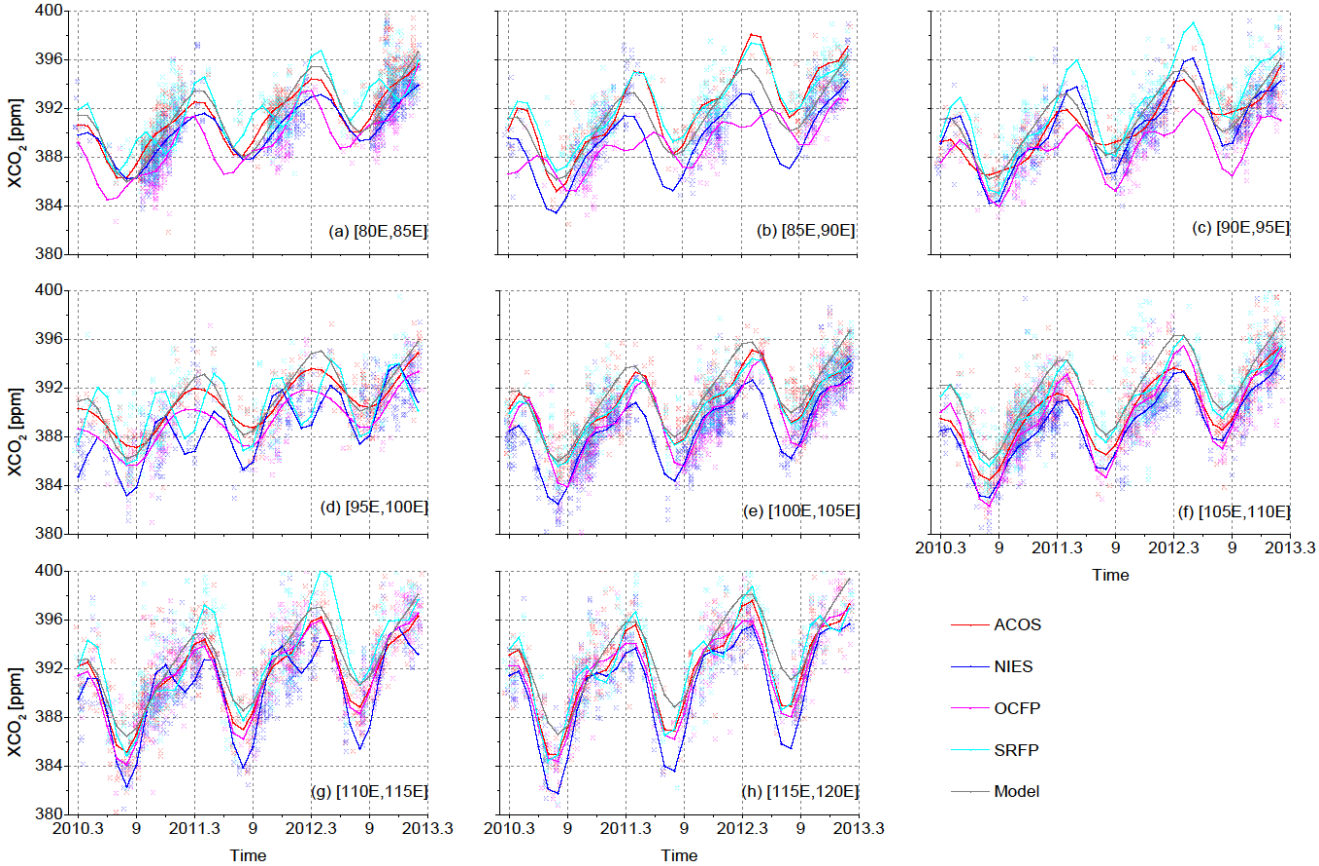

Fig. 7: The time series from March 2010 to February 2013 in eight cells from the western cell of (a) to the eastern end cell of (h), where colored lines represent the fitting seasonal change trend of the four XCO_2 datasets from the four algorithms, and the colored points represent single XCO_2 retrievals corresponding to four algorithms according to line color: red is for ACOS, blue for NIES, magenta for OCFP and cyan for SRFP. The gray line is the fitting seasonal change trend of XCO_2 simulated by GEOS-Chem.

Table 6: Results of fitted seasonal cycle and the corresponding uncertainty of the fitting results for each cell in the study latitude band for four algorithms and GEOS-Chem, The symbols "–" means that filtered results are not available due to large uncertainty judged by R and σ. R, the correlation coefficient between fitted XCO2 and monthly averaged original XCO2 in each cell, less than 0.80, and σ , the unit weighted mean square error in fitting, not less than 3.0, are highlighted in bold and underlined.

Left longitude of cells (°E)	80	85	90	95	100	105	110	115
Seasonal cycle amplitude (ppm)								
ACOS	5.1	7.8	3.7	4.0	6.6	5.9	8.0	9.3
NIES	4.3	6.9	7.8	-	7.1	6.4	9.5	10.7
OCFP	5.3	3.5	-	3.9	7.7	9.2	8.4	8.6
SRFP	6.3	6.5	8.9	-	5.9	7.4	10.4	10.7
GEOS-Chem	6.3	5.9	5.7	5.6	6.5	6.9	7.2	7.9
σ(Unit weight mean square error in fitting)(ppm)								
ACOS	1.2	1.6	1.6	0.6	1.1	1.2	0.4	1.0
NIES	0.7	1.1	1.0	**3.0**	1.1	1.1	1.5	1.3
OCFP	0.7	0.9	1.5	1.4	1.9	1.1	0.8	0.9
SRFP	1.6	0.7	1.3	**3.3**	0.8	0.8	1.0	1.0
GEOS-Chem	0.1	0.1	0.1	0.1	0.1	0.1	0.1	0.1
R (Correlations between fitted XCO2 and monthly averaged original XCO2 in each cell)								
ACOS	0.92	0.92	0.91	0.95	0.91	0.91	0.98	0.94
NIES	0.89	0.91	0.94	**0.68**	0.96	0.95	0.89	0.92
OCFP	0.90	0.84	**0.79**	0.84	0.93	0.93	0.93	0.96
SRFP	0.83	0.94	0.92	**0.40**	0.95	0.94	0.93	0.90
GEOS-Chem	1.00	1.00	0.99	0.99	0.99	0.99	0.99	0.99

Viewing the attribution of XCO_2 in each cell from Fig. 7 and Table 6, we can find that the seasonal variations from all XCO_2 retrievals generally show similar changing trends, except for one extra seasonal cycle maximum being misidentified in some cases mainly due to weaker data constraints for fitting. The timely changing patterns (indicated by seasonal cycle phases) of all algorithms demonstrate better agreement in the eastern four cells from 100°E to 115°E than those in the western four cells from 80°E to 95°E. The correlation coefficients of fitting XCO_2 in Table 6 are also significantly greater in the eastern four cells than those in the western four cells. As a result, the longitude 100°E tends to be a regional border presenting better consistency of XCO_2 among the four algorithms in its eastern cells than those in its western cells.

Comparing XCO_2 from the four algorithms with GEOS-Chem, one specific result is presented in the eastern-most two cells from 110°E to 120°E, in which the seasonal amplitudes of XCO_2 are significantly higher from the four algorithms while the magnitudes of XCO_2 in summer are lower than those from GEOS-Chem as shown in Table 6 and Fig. 7. There is strong

CO2 absorption from farming activities of wheat and corn in the summer (Lei et al., 2010) and anthropogenic CO_2 emission from extra winter heating in these eastern cells. This result is in agreement with an investigation of results over the whole Chinese mainland (Lei et al., 2014) and at 120-180°E over the globe (Lindqvist et al., 2015), which is likely due to the underestimated widespread bio-ecological CO_2 uptake changes that occurred over the past 50 years in atmospheric transport models (Graven et al., 2013).

The XCO_2 values from NIES (blue in Fig. 7) are overall lower than those from the other algorithms, which is due to the uncorrected systematic errors -1.2 ppm (refer to Table 1). The seasonal variations from OCFP (magenta in Fig. 7) are abnormal compared to the overall seasonal changing trend of XCO_2 in cells west of 100°E presented for the other three algorithms. The seasonal amplitudes of OCFP presented in Table 6, moreover, are abnormally the lowest in a cell (85-90°E) and the highest in a cell (105-110°E). SRFP and NIES show two abnormal peaks in a cycle of a year in the cell of 95°E, while some large values of σ and small values of R, shown in bold in Table 6, indicate poor fitting mostly in the same cell (95-100°E). These results are likely induced by large gaps in the available XCO_2 data in time series, which leads to a poor fitting constraint.

4.2 Spatio-temporal pattern of detrended XCO_2

We calculated the seasonal averages of the XCO_2 background concentration in each cell after removing the linear yearly increase using the fitting time series of XCO_2 for the four algorithms and GEOS-Chem. The spatio-temporal continuous pattern of background XCO_2 was mapped by Linearly Interpolate Triangulation (Watson et al., 1984) using the seasonal averages of XCO_2 background concentration in each cell for four algorithms and GEOS-Chem, as shown in Fig. 8 (on the left). The spatio-temporal patterns of the differences of detrended XCO_2 to GEOS-Chem simulations for the four algorithms are mapped respectively and are shown in Fig. 8 (on the right).

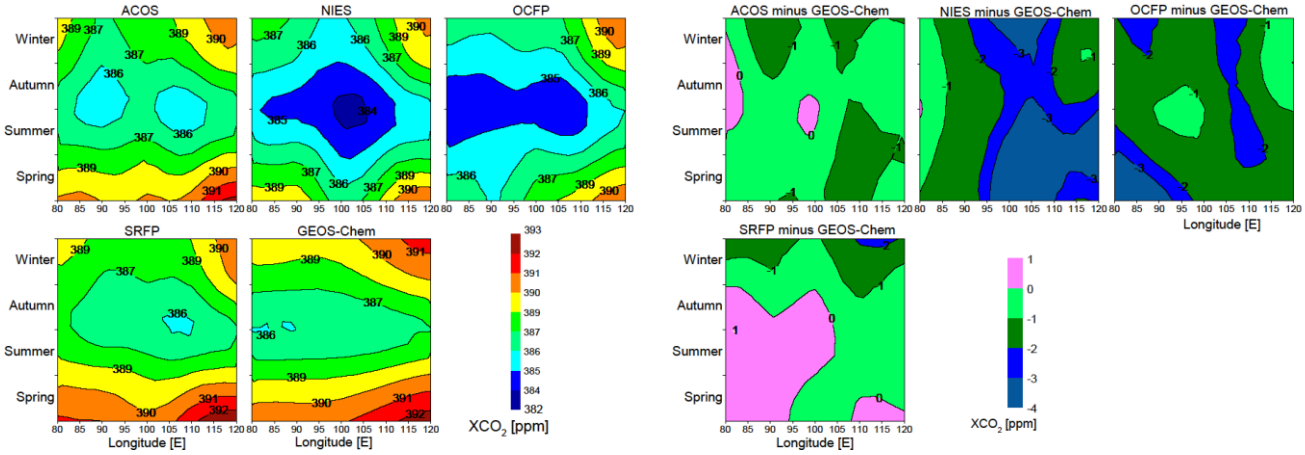

Fig. 8: The spatial (in the study latitude band) and temporal (in seasons) changing patterns of detrended XCO_2 from ACOS, NIES, OCFP, SRFP retrievals and GEOS-Chem simulations (left) and the differences of detrended XCO_2 to GEOS-Chem for ACOS, NIES, OCFP and SRFP.

It can be seen from Fig. 8 (on the left) that the spatio-temporal patterns from the three algorithms of ACOS, NIES and SRFP are generally similar, with an increase spreading outward from the center of each diagram and with the lowest XCO_2 located approximately at 95 °E-105 °E and during the period of summer-autumn; meanwhile, OCFP and GEOS-Chem show a similar spatio-temporal pattern where the lowest value is not the center. Two common characteristics of XCO_2 spatio-temporal changes from the four algorithms and GEOS-Chem can also be found: (1) the seasonal changes of XCO_2 are the same in any of the cells, with lower XCO_2 in summer and autumn than that in spring and winter; and (2) spatial changes of XCO_2 generally demonstrate larger XCO_2 in the eastern cells than those in the western cells in all seasons. A similarly high level is captured by ACOS, NIES and SRFP generally in the western deserts with lower CO_2 emissions compared to the eastern cells with abundant emissions. This feature is especially distinct from ACOS while OCFP and GEOS-Chem both show an increasing trend from west to east in any season.

Comparing the difference to GEOS-Chem (on the right in Fig. 8), the spatio-temporal pattern of ACOS and SRFP generally demonstrate the smallest values mostly ranging from -1 ppm to 1 ppm. XCO_2 values from both NIES and OCFP are smaller than GEOS-Chem in space and time, while the XCO_2 difference is mostly 1-3 ppm for NIES and 2 ppm for OCFP. Regionally, the differences tend to be larger in the western cells than those in the eastern cells for satellite retrievals, except for OCFP.

5 Discussion

In this section, an investigation was made into the most likely attribution of regional inconsistency, i.e., aerosols and albedo, and an additional comparison was made with the latest released ACOS V7.3, the newer version of ACOS data retrieved by

the OCO-2 algorithm, using GEOS-Chem simulations and retrievals from other algorithms including ACOS V3.5, NIES V02.21, OCFP V6.0 and SRFP V2.3.7.

5.1 Discussion of albedo and aerosol effects for XCO_2 retrieval

The above quantification and analyses indicate that generally good agreements are achieved among the four data sets in the eastern cells, while three out of four GOSAT-XCO_2 data sets present abnormal high concentrations in the western cells. It has been known that aerosols are the most important factor inducing errors in satellite-retrieved XCO_2 (Guerlet et al., 2013; Oshchepkov et al., 2013; Yoshida et al., 2013; O'Dell et al., 2012), while estimations of Aerosol Optical Depth (AOD) in GOSAT full physics CO2 retrieval algorithms are greatly affected by high surface albedo because of atmospheric multiple scattering of light and the optical lengthening effect. For that reason, we investigate the spatial and temporal characteristics of aerosols and albedo in our study latitude band to probe the reason why high inconsistency of XCO_2 retrieval algorithms appears in western cells rather than in eastern cells with intensive human activities.

The spatial and temporal characteristics of shortwave broadband (300-3000nm) albedo from GLASS albedo products and AOD at 555 nm from MISR aerosol products with seasons in the study area are revealed as shown in Fig. 9, in which they are mapped by the same method as Fig. 8. The seasonal mean AOD and albedo were calculated in spring (MAM), summer (JJA), autumn (SON), and winter (DJF) using the monthly mean AOD and black sky shortwave albedo from January 2010 to December 2012 for every cell.

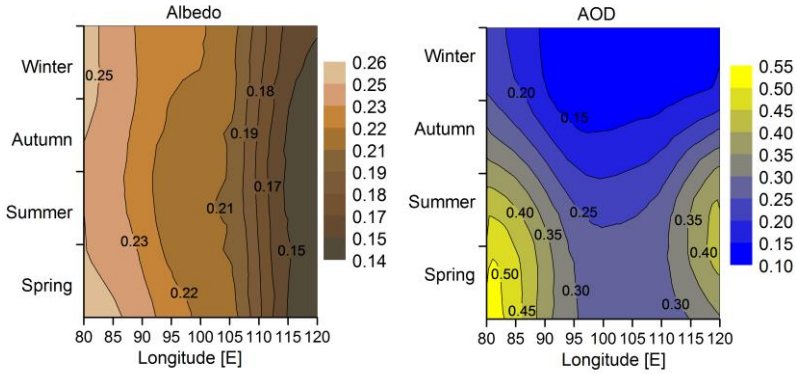

Fig. 9: The temporal and spatial patterns of black sky shortwave broadband (300-3000nm) albedo (left) and AOD at 555 nm (right). Colors represent albedo (left) and AOD (right).

As shown in Fig. 9, albedo shows small temporal variation with a decreasing trend from west to east. In contrast with albedo, AOD follows a clear seasonal pattern with a higher level in spring and summer than in autumn and winter. The uplift of AOD in spring and summer is due to the higher frequency of Asian sand and dust storms for cells west of 105 °E. The main contributors to aerosol loading east of 110 °E are emissions from urban fugitive dust/fly ash, dust plumes from deserts in the western and northern China such as the Taklimakan deserts, industrial activities and residential heating (Zhang et al.,

2012). For this reason the inconsistency of XCO_2 from the four algorithms, which tends to be higher in spring and summer than in autumn and winter in the Taklimakan Deserts in western cells shown in the results above, is likely induced by the combined effect of high aerosol and high brightness surface (high surface albedo) on retrieval uncertainty.

We discussed the influences of albedo and AOD on XCO_2 retrievals from ACOS, NIES, OCFP and SRFP in further. Fig. 10 plots the scatters of albedo and AOD with the differences between GEOS-XCO2 data (created in section 3.1) to XCO_2 retrievals, hereafter referred to as $dmXCO_2$, for ACOS, NIES, OCFP and SRFP. The albedo data obtained from GLASS02B06 is used for OCFP as there are no albedo data available from its released data product.

Fig. 10 shows that $dmXCO_2$ of both ACOS and NIES demonstrate a slightly decreasing trend with albedo whereas slightly increasing trend with AOD. The $dmXCO_2$ of ACOS tend to be larger in 80°E -90°E of deserts with high albedo than that in other regions. The dmXCO2 of OCFP demonstrate a clear decreasing trend with albedo and AOD comparing to the other algorithms. The $dmXCO_2$ of SRFP basically does not show a clearly dependence on either albedo or AOD. We further investigated the standard deviation of $dmXCO_2$ by a variation of the bin-to-bin $dmXCO_2$ with albedo and AOD. $dmXCO_2$ is averaged by surface albedo within 0.05 albedo bins and AOD within 0.05 AOD bins, respectively. The standard deviation of the mean $dmXCO_2$ in each 0.05 albedo (AOD) bins, i.e. a measure of the bin-to-bin $dmXCO_2$, is calculated. It is found that the dmXCO2 for the four algorithms change with both albedo and AOD in bin-to-bin. In the whole study area, the standard deviation in albedo is the largest for OCFP, up to 0.7 ppm, while that is smaller from ACOS, NIES and SRFP, 0.4 ppm、0.3 ppm and 0.2 ppm, respectively. The standard deviation of $dmXCO_2$ in AOD is larger for SRFP (0.5 ppm) than those for ACOS (0.2 ppm), NIES (0.3 ppm) and OCFP (0.4 ppm). Viewing to the deserts (80°E -90°E), the standard deviation in albedo is the largest from NIES (1.5 ppm), and the smallest from OCFP (0.2 ppm) while they are 1.0 ppm and 0.5 ppm for ACOS and SRFP, respectively. The standard deviations in AOD, however, are similar (0.2-0.4 ppm) in this area. As a result, OCFP tend to be more sensitive to albedo and AOD compared to other algorithms. In the deserts, NIES are the most sensitive XCO_2 retrievals to surface albedo and OCFP the least.

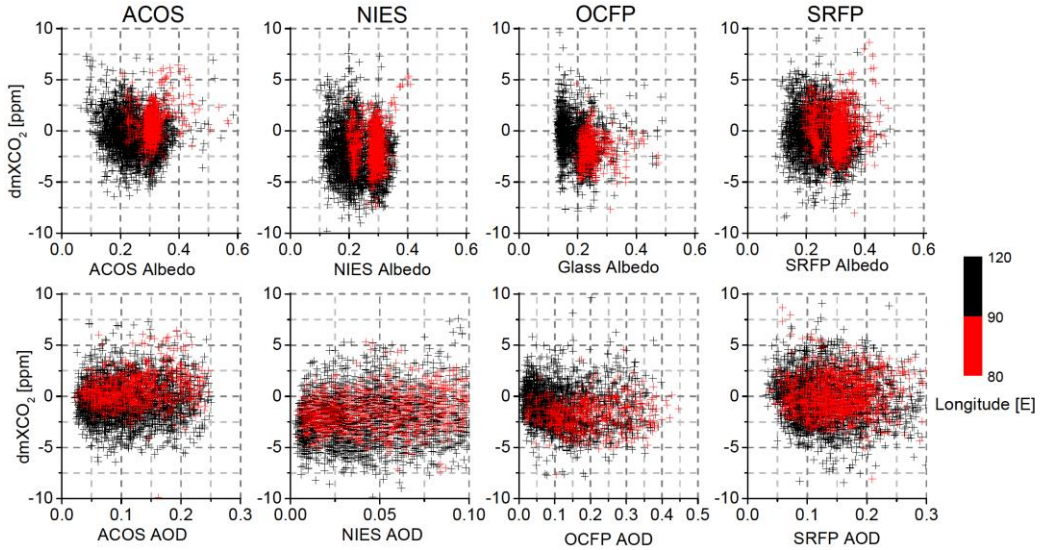

Fig. 10: Scatter plots of the differences ($dmXCO_2$) between GEOS-XCO_2 to ACOS, NIES, OCFP and SRFP respectively, with respect to albedo (the upper panels) and AOD (the lower panels). Colored points represent the data from different cells: red-[80 °E, 105 °E], black-[105 °E, 120 °E] in the study latitude zone [37 °N, 42 °N]. Colored solid lines display the corresponding linear regression trend line for the total points. Albedo and AOD are extracted from data products of the retrieval algorithms except albedo data in OCFP in which GLASS data are used.

Fig. 11, moreover, demonstrates the influence of albedo and AOD on the standard deviation (STD) of XCO_2 from four algorithms at the same footprints (timely in the same day, geometrically located within $\pm 0.01°$ in space). Averaged albedo (the left panels) and AOD (the right panels) of the four algorithms are used whereas the averaged albedo is obtained only using three attached albedo in the algorithms except OCFP.

The increasing trends of STD with both albedo and AOD can be seen from Fig. 11. The mean STD is 1.3 ppm in the western cells (80°E -90°E) where albedo is mostly within 0.25-0.35. This STD is lightly larger than that (1.0ppm) in eastern cells (90°E-120E°) where albedo is comparatively smaller (mostly within 0.15-0.25). It is found from the statistics presented in Fig. 11 that the correlation coefficients of STD with albedo and that with AOD is almost the same (both are 0.3) for all the data. Particular influence from albedo in desert over the western cells can be clearly observed. These results indicate that the inconsistency of XCO_2 retrievals from four algorithms tend to be increase with the enlargements of albedo and AOD so as to imply that uncertainty of satellite-retrieved XCO_2 should be mostly alerted with the elevations of albedo and AOD.

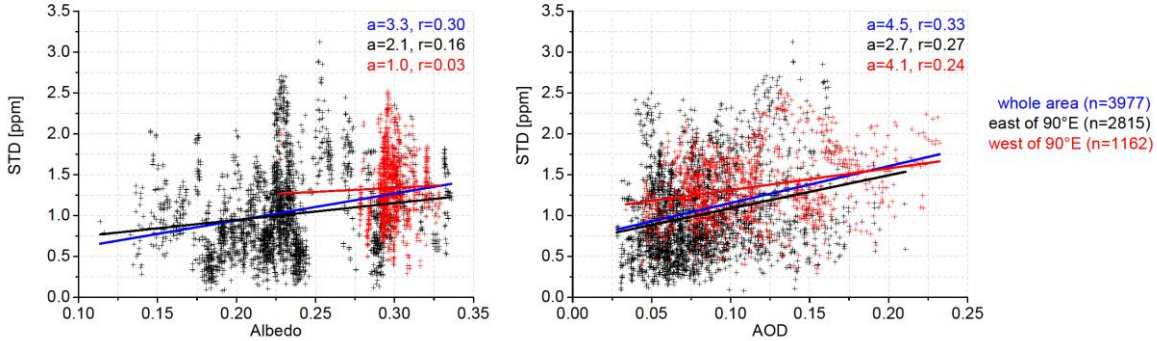

Fig. 11: Scatter plots of the standard deviation (STD) of XCO_2 from the four algorithms to albedo (the left panel) and AOD (the right panel). Colored points represent different cells: red-[80 °E, 105 °E], black-[105 °E, 120 °E] in the latitude zone [37 °N, 42 °N]. Colored solid lines display the corresponding linear regression trend line for the scatter plots with the regression slope (a) and the correlation coefficient (r) also presented. n is the number of samples. Albedo is the mean surface albedo in 0.75-um band from the three algorithms including ACOS, NIES and SRFP. AOD is the mean AOD in 0.75-um band from the four algorithms.

From the above quantification and analysis in previous sections, the pairwise differences between OCFP and other algorithms are 0.5 ppm higher west of 105 °E than east of that, with a difference of 1.2 ppm over the whole study area. The obvious regional characteristic probably relates to the assumption of a uniform cirrus profile based on latitude in the retrieval algorithm (GHG-CCI group at University of Leicester, 2014), which is, however, unlikely to be reasonable in our study area. There exists a large amount of high clouds over the Tibetan Plateau (Chen et al., 2005), which is located south of the study cells of 80 °E to 105 °E. The humidity and atmospheric structure are mainly affected by the Tibetan Plateau, and there is a large difference in the cirrus profile between the western cells and the eastern cells over our study area (Wang et al., 2012), which indicates that a uniform profile by latitude will inevitably introduce errors.

The regional pairwise difference between NIES and other algorithms is up to 1.6 ppm, which is distinctly high among all the algorithms. Considering the complicated geographic environment in the study area, this distinct difference is likely related to the presumptions from NIES algorithm in aerosol profiles and properties adopted from an aerosol transport model (Table 1), in which cirrus clouds are ignored and little information from observations is used in the retrieving process.

With the satellite-observed spectrum used for simultaneously retrieving water and clouds, ACOS sets the initial aerosol types and AOD based on a priori information from aerosol reanalysis data. On the other hand, SRFP handles aerosol based on a comprehensive characterization of aerosol properties, including aerosol number density, size distribution and aerosol height. Both of the above two mechanisms function well since ACOS and SRFP are generally demonstrated to provide relatively better performance.

Noticing that all algorithms differ in simulating scattering in the atmosphere, such as in the aerosol models, the influence of scattering on retrieved XCO_2 is too significant to be ignored, as demonstrated from this study. Since satellite products from different retrieval algorithms in general agree with each other, there is no denying that satellite XCO_2 retrievals have the potential to provide more accurate XCO_2 data. Optimization in the handling of aerosol scattering will improve the precision and accuracy of satellite XCO_2 retrievals in the future.

5.2 Additional comparison with the latest released ACOS V7.3

We collected ACOS V7.3 (http://CO2.jpl.nasa.gov) too, the latest version of the ACOS data (GES DISC, 2017). We add the cross-comparisons of this version of the data set and other data sets including GEOS-Chem, ACOS V3.5, NIES V02.21, OCFP V6.0 and SRFP V2.3.7 in this section. ACOS V7.3 was created by applying the XCO_2 retrieval algorithms of OCO-2 to GOSAT. Within the algorithm code of ACOS V3.5, the OCO-2 algorithm generating ACOS V7.3 data makes some changes in parameter settings, such as the surface pressure a priori constraint and cloud ice properties, and it updates the manners of data processing, for example, the bias corrections and filtering mechanism (GES DISC, 2017).

Compared to the previous version, ACOS V3.5, ACOS V7.3 increases the average by approximately 0.2 ppm. In comparison with the difference patterns with ACOS V3.5, the averages of the absolute differences between ACOS V7.3 and the other three algorithms are similar (within 0.1 ppm) and increase by an average of 0.5 ppm (1.8 ppm vs. 1.3 ppm) in cells east of 110 °E and west of 90 °E, respectively, while the biases relative to GEOS-Chem decrease approximately 0.3 ppm and increase approximately 0.9 ppm in cells east and west of 90 °E, respectively.

The comparison results further demonstrate inconsistency of XCO_2 among different datasets in the desert cells.

6 Conclusion

Although TCCON has been widely accepted as the standard for validation of satellite-based XCO_2 data, it is necessary to better understand the performance of XCO_2 in spatial and timely variations at a regional scale and especially for those regions where ground-based measurements of XCO_2 are not available, such as for the TCCON stations in China. We implement the quantification and assessment of the agreement of multiple algorithms for typical regions with various land covers and enhancement of anthropogenic CO_2 emissions including the megacity of Beijing from 80 °E to 120 °E in the same latitude band of 40 °N to get better knowledge of the regional uncertainty and performance of GOSAT XCO_2 retrievals in China. Regional performance of XCO_2 products from four algorithms (ACOS, NIES, OCFP, SRFP) as well as GEOS-Chem simulated XCO_2 are probed to obtain the regional uncertainty and attributions of GOSAT XCO_2 retrievals. In particular, we apply simulated XCO_2 at a high spatial resolution of 0.5 °(latitude) x 0.666 °(longitude) for a nested grid obtained by GEOS-Chem to assess the regional uncertainty of XCO_2 derived from satellite observations in China. In connection with the inconsistency of algorithms in eight cells, the characteristics of aerosol and albedo are investigated to discuss the further attribution of regional inconsistency of algorithms.

Summarizing the performance of four algorithms (ACOS, NIES, OCFP and SRFP) in each cell based on the above quantification and analysis from comparisons with GEOS-Chem, pairwise differences between algorithms and agreement in time series among algorithms, we can obtain the following results in general: (1)The consistency among algorithms is better in the east than in the west as the absolute difference from pairwise comparisons presents 0.7-1.1 ppm in eastern cells covered by grassland, cropland and built-up areas with strong anthropogenic CO_2 emission whereas 1.0-1.6 ppm in western cells covered by desert with a high-brightness surface with less anthropogenic CO_2 emission; （2）ACOS and SRFP are

more satisfying in characterizing spatio-temporal patterns than other algorithms. To conclude, Table 7 presents the regional characteristics and a summary of the results described in above sections.

Table 7. Summaries of our analyses for uncertainty of XCO2 retrievals obtained by GOSAT via inter-comparison of multi-algorithms above, including characteristics of regional emissions, albedo, aerosol optical depth, and summary of differences between algorithms and bias compared to GEOS-Chem.

Characteristics of regions and summary of algorithms		Cells from 80 °E to 115 °E within 37°N-42°N							
Characteristics of regions	Regions Left longitude (°E)	80	85	90	95	100	105	110	115
	CO_2 emissions (Tg/year)*[1]	Low emissions (1.2-57.1)					High emissions (515.2-**821.9**)		
	Property of aerosol (AOD)*[2]	Dust (0.22-**0.53)**		Clear (0.10-0.28)				Urban (0.10-0.37))	
	Surface types (albedo)	Sand desert with high brightness (0.20-**0.26**)			Gobi and grassland (0.19-0.22)			Cropland and built-up (0.14-0.17)	
Summary of uncertainty	Consistency of algorithms (pairwise mean absolute differences)	Less Consistency (1.0-1.6 ppm)					Good consistency (0.7-1.1 ppm)		
	Bias compared to GEOS-Chem (bias range)	Large biases (1.2-3.1 ppm)						lesser biases excluding NIES (0.0-0.5 ppm)	
	General performance of algorithms in spatio-temporal patterns of XCO_2 compared to GEOS-Chem	ACOS presents the lowest bias (-0.1±1.9 ppm); SRFP is next (-0.2±2.2 ppm) NIES presents the greatest -2.0±2.2 ppm)							

*[1] represents the total emissions of CO_2 from CHRED in each cell in 2012. *[2] is the range of averaged seasonal aerosol optical depth over a year.

The results of our analysis, indicating that the discrepancies among algorithms are the smallest in eastern cells which are the strongest anthropogenic emitting source regions in China, implies that the uncertainty of XCO_2 is likely low in this area. It will be sufficiently rigorous for supporting us to apply GOSAT XCO_2 data in assessment of anthropogenic emissions via timely changing magnitude of XCO_2 in such region. Moreover, it was likely that uncertainty in satellite-retrieved XCO_2 is attributed to the combined effects of aerosol and albedo. The large uncertainty of XCO_2 must be improved further, even though many algorithms have endeavored to minimize the effects of aerosol and albedo. With the launch of OCO-2 in 2014 and GOSAT-2 scheduled for 2018, the prospect of a large amount of useful retrieved XCO_2 products is promising. Since low regional XCO_2 biases are necessary for accurately estimating regional carbon sources and sinks, regional uncertainty should be paid more attention in the future.

Appendix A

We made cross-comparisons between ACOS V7.3 and other data sets. The available data points of ACOS V7.3 were shown from March 2010 to February 2013 in Fig.A1. In cells west of 90 °E, there are a few data points showing abnormal concentrations as high as above 400.0 ppm, which is higher than that of data points in the east, where there are strong anthropogenic CO_2 emissions.

The comparison results in the cells are shown in Table A1. No bias was found in ACOS V7.3 from GEOS-Chem with a standard deviation of 1.6 ppm and R^2 of 0.77 in the whole study area. Generally, ACOS V7.3 is in good agreement with all of them, which is reflected by correlation coefficients r that are above 0.85 and greater than others, as shown in Table A1. The biggest differences up to 3.0 ppm for ACOS V7.3 are found from NIES and OCFP in deserts cells, whereas differences from SRFP are mostly within 1.0 ppm. This is similar to ACOS V3.5. The pairwise differences from other algorithms (not including ACOS V3.5) are up to 1.9 ppm in cells west of 90 °E, which is distinctly high, whereas within 0.9 ppm in cells east of 110 °E. It can also be found that the bias of ACOS V7.3 relative to GEOS-Chem is within 0.3 ppm but above 1.3 ppm, in cells east and west of 90 °E, respectively.

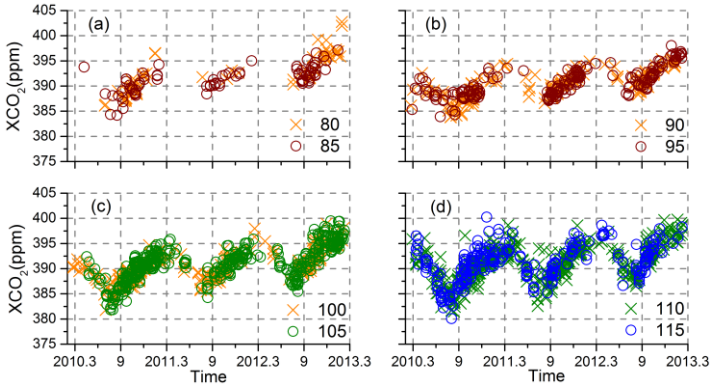

Fig. A1. The time series of data points from ACOS V7.3 during the period from March 2010 to February 2013. Different symbols in each panel represent the left longitude of the cell into which a data point falls.

Table A1. Differences between ACOS V7.3 and others (including GEOS-Chem and four other algorithms including ACOS V3.5, NIES, OCFP and SRFP) in each cell (subtraction from ACOS V7.3). Values in parentheses are the corresponding standard deviations.

Left longitude of cells(°E)	80	85	90	95	100	105	110	115	r
GEOS-Chem	**-1.7**(1.5) 64	-1.3(1.3) 85	0.1(1.2) 167	0.1(1.2) 191	-0.1(1.3) 294	0.3(1.6) 448	0(1.7) 487	0(1.6) 244	0.88
ACOS V3.5	-0.4(0.9) 103	-0.1(1.0) 48	-0.1(1.0) 133	-0.2(1.0) 189	0.0(1.1) 350	-0.5(1.1) 391	0.2(1.2) 244	-0.1(1.1) 126	0.93
NIES	**-3.2**(1.2) 61	**-1.9**(1.5) 100	**-1.6**(1.2) 251	-1.2(1.9) 123	**-1.9**(1.4) 541	**-1.8**(1.5) 317	-1.2(1.6) 397	-0.7(1.5) 277	0.87
OCFP	**-3.1**(1.0) 66	**-3.4**(0.9) 41	**-2.2**(1.1) 157	**-2.5**(1.5) 114	**-2.1**(1.2) 297	-1.5(1.1) 329	-0.5(1.1) 396	-0.1(1.0) 202	0.86
SRFP	-0.8(1.3) 138	-0.7(1.4) 145	0.3(1.3) 345	-0.6(1.3) 337	-0.4(1.3) 466	-0.5(1.4) 631	0.3(1.4) 447	0.1(1.2) 247	0.89
Average absolute difference[1] for three algorithms above	1.9(1.5)	1.7(1.4)	1.2(1.0)	1.4(1.1)	1.3(1.0)	1.2(0.8)	0.9(0.7)	0.7(0.5)	

***[1] represents the average of absolute differences of ACOS V7.3 matching other algorithms including NIES, OCFP and SRFP for each cell.**

Acknowledgements: This research was supported by the National Research Program on Global Changes and Adaptation: "Big data on global changes: data sharing platform and recognition" (Grant No. 2016YFA0600303, 2016YFA0600304). We are grateful for NIES products from NIES GOSAT Project, albedo data from Beijing Normal University, XCO_2 data from the TCCON data archive, operated by the California Institute of Technology, and supports from GEOS-Chem team. ACOS V3.5 and ACOS V7.3 were produced by the ACOS/OCO-2 project at the Jet Propulsion Laboratory, California Institute of Technology, and obtained from the JPL website, http://CO2.jpl.nasa.gov . We are grateful for aerosol data from Aeronautics and Space Administration (NASA). The satellite XCO_2 products OCFP and SRFP have been obtained from the ESA project GHG-CCI website (http://www.esa-ghg-cci.org/) and the data providers Univ. Leicester (OCFP product) and SRON & KIT (SRFP) have granted permission to use these data for peer-reviewed publications.

References

Andres, R. J., Boden, T. A., Bréon, F. M., Ciais, P., Davis, S., Erickson, D., Gregg, J. S., Jacobson, A., Marland, G., Miller, J., Oda, T., Olivier, J. G. J., Raupach, M. R., Rayner, P., and Treanton, K.: A synthesis of carbon dioxide emissions from fossil-fuel combustion, Biogeosciences, 9, 1845-1871, https://doi.org/10.5194/bg-9-1845-2012, 2012.

Bie, N., Lei, L., He, Z., and Liu, M.: An analysis of atmospheric CO 2 concentration around the takelamagan desert with five products retrieved from satellite observations, International Geoscience and Remote Sensing Symposium (IGARSS), Beijing, China, 10-15 July 2016, https://doi.org/10.1109/IGARSS.2016.7730064, 2016.

Blumenstock, T., Hase, F., Schneider, M., Garcia, O. E. and Sepulveda, E.: TCCON data from Izana, Tenerife, Spain, Release GGG2014R0, TCCON data archive, CDIAC, https://doi.org/10.14291/tccon.ggg2014.izana01.R0/1149295, 2014.

Bovensmann, H., Burrows, J. P., Buchwitz, M., Frerick, J., Noël, S., Rozanov, V. V., Chance, K. V., and Goede, A. P. H.: SCIAMACHY: Mission Objectives and Measurement Modes, J. Atmos. Sci., 56, 127-150, 1999.

Buchwitz, M., Reuter, M., Schneising, O., Boesch, H., Guerlet, S., Dils, B., Aben, I., Armante, R., Bergamaschi, P., Blumenstock, T., Bovensmann, H., Brunner, D., Buchmann, B., Burrows, J. P., Butz, A., Chédin, A., Chevallier, F., Crevoisier, C. D., Deutscher, N. M., Frankenberg, C., Hase, F., Hasekamp, O. P., Heymann, J., Kaminski, T., Laeng, A., Lichtenberg, G., De Mazière, M., Noël, S., Notholt, J., Orphal, J., Popp, C., Parker, R., Scholze, M., Sussmann, R., Stiller, G. P., Warneke, T., Zehner, C., Bril, A., Crisp, D., Griffith, D. W. T., Kuze, A., O'Dell, C., Oshchepkov, S., Sherlock, V., Suto, H., Wennberg, P., Wunch, D., Yokota, T., and Yoshida, Y.: The Greenhouse Gas Climate Change Initiative (GHG-CCI): Comparison and quality assessment of near-surface-sensitive satellite-derived CO_2 and CH_4 global data sets, Remote Sens. Environ., 162, 344-362, http://dx.doi.org/10.1016/j.rse.2013.04.024 , 2015.

Burrows, J. P., Hölzle, E., Goede, A. P. H., Visser, H., and Fricke, W.: SCIAMACHY—scanning imaging absorption spectrometer for atmospheric chartography, Acta Astronaut., 35, 445-451, https://doi.org/10.1016/0094-5765(94)00278-T , 1995.

Butz, A., Guerlet, S., Hasekamp, O., Schepers, D., Galli, A., Aben, I., Frankenberg, C., Hartmann, J. M., Tran, H., Kuze, A., Keppel-Aleks, G., Toon, G., Wunch, D., Wennberg, P., Deutscher, N., Griffith, D., Macatangay, R., Messerschmidt, J., Notholt, J., and Warneke, T.: Toward accurate CO_2 and CH_4 observations from GOSAT, Geophys. Res. Lett., 38, n/a-n/a, https://doi.org/10.1029/2011gl047888 , 2011.

Cai, B., and Zhang, L.: Urban CO_2 emissions in China: Spatial boundary and performance comparison, Energy Policy, 66, 557-567, https://doi.org/10.1016/j.enpol.2013.10.072 , 2014.

Chen, B.: Seasonal migration of cirrus clouds over the Asian Monsoon regions and the Tibetan Plateau measured from MODIS/Terra, Geophys. Res. Lett., 32, https://doi.org/10.1029/2004gl020868, 2005.

Ciais, P., Rayner, P., Chevallier, F., Bousquet, P., Logan, M., Peylin, P., and Ramonet, M.: Atmospheric inversions for estimating CO_2 fluxes: methods and perspectives, Climatic Change, 103, 69-92, https://doi.org/10.1007/s10584-010-9909-3, 2010.

Cogan, A. J., Boesch, H., Parker, R. J., Feng, L., Palmer, P. I., Blavier, J. F. L., Deutscher, N. M., Macatangay, R., Notholt, J., Roehl, C., Warneke, T., and Wunch, D.: Atmospheric carbon dioxide retrieved from the Greenhouse gases Observing

SATellite (GOSAT): Comparison with ground-based TCCON observations and GEOS-Chem model calculations, J. Geophys. Res. Atmos., 117, n/a-n/a, https://doi.org/10.1029/2012jd018087, 2012.

Connor, B. J., Boesch, H., Toon, G., Sen, B., Miller, C., and Crisp, D.: Orbiting Carbon Observatory: Inverse method and prospective error analysis, J. Geophys. Res. Atmos., 113, n/a-n/a, https://doi.org/10.1029/2006jd008336, 2008.

Detmers, R., Hasekamp, O.: Product User Guide (PUG) for the RemoTeC XCO2 Full Physics GOSAT Data Product, available at http://www.esa-ghg-cci.org/sites/default/files/documents/public/documents/GHG-CCI_DATA.html, 2015.

Deutscher, N., Notholt, J., Messerschmidt, J., Weinzierl, C., Warneke, T., Petri, C., Grupe, P. and Katrynski, K.: TCCON data from Bialystok, Poland, Release GGG2014R1, TCCON data archive, CDIAC, https://doi.org/10.14291/tccon.ggg2014.bialystok01.R1/1183984, 2014.

GHG-CCI group at University of Leicester: Algorithm Theoretical Basis Document Version 3 (ATBDv3)-The University of Leicester Full-Physics Retrieval Algorithm for the retrieval of XCO2 and XCH4, available at http://www.esa-ghg-cci.org/sites/default/files/documents/public/documents/GHG-CCI_DATA.html, 2014.

Giglio, L., Randerson, J. T., and van der Werf, G. R.: Analysis of daily, monthly, and annual burned area using the fourth-generation global fire emissions database (GFED4), J. Geophys. Res. Biogeosci., 118, 317-328, https://doi.org/10.1002/jgrg.20042, 2013.

Graven, H. D., Keeling, R. F., Piper, S. C., Patra, P. K., Stephens, B. B., Wofsy, S. C., Welp, L. R., Sweeney, C., Tans, P. P., Kelley, J. J., Daube, B. C., Kort, E. A., Santoni, G. W., and Bent, J. D.: Enhanced seasonal exchange of CO_2 by northern ecosystems since 1960, Science, 341, 1085-1089, https://doi.org/10.1126/science.1239207, 2013.

Griffith, D. W. T., Deutscher, N., Velazco, V. A., Wennberg, P. O., Yavin, Y., Aleks, G. K., Washenfelder, R., Toon, G. C., Blavier, J. F., Murphy, C., Jones, N., Kettlewell, G., Connor, B., Macatangay, R., Roehl, C., Ryczek, M., Glowacki, J., Culgan, T. and Bryant, G.: TCCON data from Darwin, Australia, Release GGG2014R0, TCCON data archive, CDIAC, https://doi.org/10.14291/tccon.ggg2014.darwin01.R0/1149290, 2014a.

Griffith, D. W. T., Velazco, V. A., Deutscher, N., Murphy, C., Jones, N., Wilson, S., Macatangay, R., Kettlewell, G., Buchholz, R. R. and Riggenbach, M.: TCCON data from Wollongong, Australia, Release GGG2014R0, TCCON data archive, CDIAC, https://doi.org/10.14291/tccon.ggg2014.wollongong01.R0/1149291, 2014b.

Goddard Earth Science Data Information and Services Center: ACOS Level 2 Standard Product Data User's Guide, v3.5, available at http://co2.jpl.nasa.gov, 2016.

Goddard Earth Science Data Information and Services Center: ACOS Level 2 Standard Product Data User's Guide, v7.3, available at http://co2.jpl.nasa.gov, 2017.

Guan, D., Liu, Z., Geng, Y., Lindner, S., and Hubacek, K.: The gigatonne gap in China/'s carbon dioxide inventories, Nature Clim. Change, 2, 672-675, https://doi.org/10.1038/nclimate1560, 2012.

Guerlet, S., Butz, A., Schepers, D., Basu, S., Hasekamp, O. P., Kuze, A., Yokota, T., Blavier, J. F., Deutscher, N. M., Griffith, D. W. T., Hase, F., Kyro, E., Morino, I., Sherlock, V., Sussmann, R., Galli, A., and Aben, I.: Impact of aerosol and thin cirrus on retrieving and validating XCO_2 from GOSAT shortwave infrared measurements, J. Geophys. Res. Atmos., 118, 4887-4905, https://doi.org/10.1002/jgrd.50332, 2013.

Hase, F., Blumenstock, T., Dohe, S., Gross, J. and Kiel, M.: TCCON data from Karlsruhe, Germany, Release GGG2014R1, TCCON data archive, CDIAC, https://doi.org/10.14291/tccon.ggg2014.karlsruhe01.R1/1182416, 2014.

Hasekamp, O., Hu, H., Detmers, R., and Butz, A.: ESA Climate Change Initiative (CCI) Algorithm Theoretical Basis Document for the RemoTeC XCO_2 and XCH_4 Full Physics Products of the Essential Climate Variable (ECV) Greenhouse Gases (GHG), available at http://www.esa-ghg-cci.org/sites/default/files/documents/public/documents/GHG-CCI_DATA.html, 2015.

He, Z., Zeng, Z.-C., Lei, L., Bie, N., and Yang, S.: A Data-Driven Assessment of Biosphere-Atmosphere Interaction Impact on Seasonal Cycle Patterns of XCO_2 Using GOSAT and MODIS Observations, Remote Sens., 9, 251, https://doi.org/10.3390/rs9030251, 2017.

Hewson, W.: Product User Guide:University of Leicester full-physics XCO2 retrieval algorithm for CRDP3 – OCFP v6.0, available at http://www.esa-ghg-cci.org/sites/default/files/documents/public/documents/GHG-CCI_DATA.html, 2016.

Kawakami, S., Ohyama, H., Arai, K., Okumura, H., Taura, C., Fukamachi, T. and Sakashita, M.: TCCON data from Saga, Japan, Release GGG2014R0, TCCON data archive, CDIAC, https://doi.org/10.14291/tccon.ggg2014.saga01.R0/1149283, 2014.

Keeling, C. D., Bacastow, R. B., Bainbridge, A. E., Ekdahl Jr., C. A., Guenther, P. R., Waterman, L. S., and Chin, J. F. S.: Atmospheric carbon dioxide variations at Mauna Loa Observatory, Hawaii, Tellus A, 28, https://doi.org/10.3402/tellusa.v28i6.11322, 2011.

Keller, C. A., Long, M. S., Yantosca, R. M., Da Silva, A. M., Pawson, S., and Jacob, D. J.: HEMCO v1.0: a versatile, ESMF-compliant component for calculating emissions in atmospheric models, Geosci. Model Dev., 7, 1409-1417, https://doi.org/10.5194/gmd-7-1409-2014, 2014.

Keppel-Aleks, G., Wennberg, P. O., O'Dell, C. W., and Wunch, D.: Towards constraints on fossil fuel emissions from total column carbon dioxide, Atmos. Chem. Phys., 13, 4349-4357, https://doi.org/10.5194/acp-13-4349-2013, 2013.

Kivi, R., Heikkinen, P. and Kyro, E.: TCCON data from Sodankyla, Finland, Release GGG2014R0, TCCON data archive, CDIAC, https://doi.org/10.14291/tccon.ggg2014.sodankyla01.R0/1149280, 2014.

Kulawik, S., Wunch, D., apos, Dell, C., Frankenberg, C., Reuter, M., Oda, T., Chevallier, F., Sherlock, V., Buchwitz, M., Osterman, G., Miller, C. E., Wennberg, P. O., Griffith, D., Morino, I., Dubey, M. K., Deutscher, N. M., Notholt, J., Hase, F., Warneke, T., Sussmann, R., Robinson, J., Strong, K., Schneider, M., De Mazière, M., Shiomi, K., Feist, D. G., Iraci, L. T., and Wolf, J.: Consistent evaluation of ACOS-GOSAT, BESD-SCIAMACHY, CarbonTracker, and MACC through comparisons to TCCON, Atmos. Meas. Tech., 9, 683-709, https://doi.org/10.5194/amt-9-683-2016, 2016.

Lei, H., and Yang, D.: Seasonal and interannual variations in carbon dioxide exchange over a cropland in the North China Plain, Glob. Chang. Biol., 16, 2944-2957, https://doi.org/10.1111/j.1365-2486.2009.02136.x, 2010.

Lei, L., Guan, X., Zeng, Z., Zhang, B., Ru, F., and Bu, R.: A comparison of atmospheric CO_2 concentration GOSAT-based observations and model simulations, Sci. Chin.-Earth Sci., 57, 1393-1402, https://doi.org/10.1007/s11430-013-4807-y, 2014.

Lindqvist, H., O'Dell, C. W., Basu, S., Boesch, H., Chevallier, F., Deutscher, N., Feng, L., Fisher, B., Hase, F., Inoue, M., Kivi, R., Morino, I., Palmer, P. I., Parker, R., Schneider, M., Sussmann, R., and Yoshida, Y.: Does GOSAT capture the true seasonal cycle of carbon dioxide?, Atmos. Chem. Phys., 15, 13023-13040, https://doi.org/10.5194/acp-15-13023-2015 , 2015.

Liu, D., Lei, L., Guo, L., and Zeng, Z.-C.: A Cluster of CO2 Change Characteristics with GOSAT Observations for Viewing the Spatial Pattern of CO_2 Emission and Absorption, Atmosphere, 6, 1695-1713, https://doi.org/10.3390/atmos6111695, 2015.

Liu, Z., Guan, D., Wei, W., Davis, S. J., Ciais, P., Bai, J., Peng, S., Zhang, Q., Hubacek, K., Marland, G., Andres, R. J., Crawford-Brown, D., Lin, J., Zhao, H., Hong, C., Boden, T. A., Feng, K., Peters, G. P., Xi, F., Liu, J., Li, Y., Zhao, Y., Zeng, N., and He, K.: Reduced carbon emission estimates from fossil fuel combustion and cement production in China, Nature, 524, 335-338, https://doi.org/10.1038/nature14677, 2015.

Messerschmidt, J., Parazoo, N., Wunch, D., Deutscher, N. M., Roehl, C., Warneke, T., and Wennberg, P. O.: Evaluation of seasonal atmosphere–biosphere exchange estimations with TCCON measurements, Atmos. Chem. Phys., 13, 5103-5115, https://doi.org/10.5194/acp-13-5103-2013, 2013.

Morino, I., Matsuzaki, T. and Shishime, A.: TCCON data from Tsukuba, Ibaraki, Japan, 125HR, Release GGG2014R1, TCCON data archive, CDIAC, https://doi.org/10.14291/tccon.ggg2014.tsukuba02.R1/1241486, 2014.

Nassar, R., Jones, D. B. A., Suntharalingam, P., Chen, J. M., Andres, R. J., Wecht, K. J., Yantosca, R. M., Kulawik, S. S., Bowman, K. W., Worden, J. R., Machida, T., and Matsueda, H.: Modeling global atmospheric CO_2 with improved emission inventories and CO_2 production from the oxidation of other carbon species, Geosci. Model Dev., 3, 689-716, https://doi.org/10.5194/gmd-3-689-2010, 2010.

Nassar, R., Napier-Linton, L., Gurney, K. R., Andres, R. J., Oda, T., Vogel, F. R., and Deng, F.: Improving the temporal and spatial distribution of CO_2 emissions from global fossil fuel emission data sets, J. Geophys. Res. Atmos., 118, 917-933, https://doi.org/10.1029/2012jd018196, 2013.

National Institute for Environmental Studies, GOSAT Project Office: NIES GOSAT TANSO-FTS SWIR Level 2 Data Product Format Description Version 2.50, available at https://data2.gosat.nies.go.jp/doc/document.html#Document, 2015.

Oda, T., and Maksyutov, S.: A very high-resolution (1 km×1 km) global fossil fuel CO_2 emission inventory derived using a point source database and satellite observations of nighttime lights, Atmos. Chem. Phys., 11, 543-556, https://doi.org/10.5194/acp-11-543-2011, 2011.

O'Dell, C. W., Connor, B., Bösch, H., O'Brien, D., Frankenberg, C., Castano, R., Christi, M., Eldering, D., Fisher, B., Gunson, M., McDuffie, J., Miller, C. E., Natraj, V., Oyafuso, F., Polonsky, I., Smyth, M., Taylor, T., Toon, G. C., Wennberg, P. O., and Wunch, D.: The ACOS CO_2 retrieval algorithm – Part 1: Description and validation against synthetic observations, Atmos. Meas. Tech., 5, 99-121, https://doi.org/10.5194/amt-5-99-2012, 2012.

Oshchepkov, S., Bril, A., Yokota, T., Wennberg, P. O., Deutscher, N. M., Wunch, D., Toon, G. C., Yoshida, Y., O'Dell, C. W., Crisp, D., Miller, C. E., Frankenberg, C., Butz, A., Aben, I., Guerlet, S., Hasekamp, O., Boesch, H., Cogan, A., Parker, R., Griffith, D., Macatangay, R., Notholt, J., Sussmann, R., Rettinger, M., Sherlock, V., Robinson, J., Kyrö, E., Heikkinen, P., Feist, D. G., Morino, I., Kadygrov, N., Belikov, D., Maksyutov, S., Matsunaga, T., Uchino, O., and Watanabe, H.: Effects of atmospheric light scattering on spectroscopic observations of greenhouse gases from space. Part 2: Algorithm intercomparison in the GOSAT data processing for CO_2 retrievals over TCCON sites, J. Geophys. Res. Atmos., 118, 1493-1512, https://doi.org/10.1002/jgrd.50146, 2013.

Sherlock, V., Connor, B., Robinson, J., Shiona, H., Smale, D. and Pollard, D.: TCCON data from Lauder, New Zealand, 125HR, Release GGG2014R0, TCCON data archive, CDIAC, https://doi.org/10.14291/tccon.ggg2014.lauder02.R0/1149298, 2014.

Sussmann, R. and Rettinger, M.: TCCON data from Garmisch, Germany, Release GGG2014R0, TCCON data archive, CDIAC, https://doi.org/10.14291/tccon.ggg2014.garmisch01.R0/1149299, 2014.

Takahashi, T., Sutherland, S. C., Wanninkhof, R., Sweeney, C., Feely, R. A., Chipman, D. W., Hales, B., Friederich, G., Chavez, F., and Sabine, C.: Takahashi, T. et al. Climatological mean and decadal changes in surface ocean pCO_2, and net sea-air CO_2 flux over the global oceans, Deep-Sea Res. Pt. II, 56, 554-577, https://doi.org/10.1016/j.dsr2.2008.12.009, 2009.

Thoning, K. W., Tans, P. P., and Komhyr, W. D.: Atmospheric carbon dioxide at Mauna Loa Observatory: 2. Analysis of the NOAA GMCC data, 1974-1985, J. Geophys. Res. Atmos., 94, 8549-8565, https://doi.org/10.1029/JD094iD06p08549, 1989.

Wang, J., Cai, B., Zhang, L., Cao, D., Liu, L., Zhou, Y., Zhang, Z., and Xue, W.: High resolution carbon dioxide emission gridded data for China derived from point sources, Environ. Sci. Technol., 48, 7085-7093, https://doi.org/10.1021/es405369r, 2014.

Wang, W., Tian, Y., Liu, C., Sun, Y., Liu, W., Xie, P., Liu, J., Xu, J., Morino, I., Velazco, V. A., Griffith, D. W. T., Notholt, J., and Warneke, T.: Investigating the performance of a greenhouse gas observatory in Hefei, China, Atmos. Meas. Tech., 10, 2627-2643, https://doi.org/10.5194/amt-10-2627-2017 , 2017..

Wang Min-zhong, H. Q., Wei Wen-shou, Yang Lian-mei, and Zhao Yong: Observational Analysis of the Troposphere and Low Stratosphere at Minfeng Station in the North Side of the Tibetan Plateau in July 2011, Plateau Meteorology, 31, 12, 2012.

Warneke, T., Messerschmidt, J., Notholt, J., Weinzierl, C., Deutscher, N., Petri, C., Grupe, P., Vuillemin, C., Truong, F., Schmidt, M., Ramonet, M. and Parmentier, E.: TCCON data from Orleans, France, Release GGG2014R0, TCCON data archive, CDIAC, https://doi.org/10.14291/tccon.ggg2014.orleans01.R0/1149276, 2014.

Watson, D. F., and Philip, G. M.: Triangle based interpolation, Mathematical Geology, 16, 779-795, https://doi.org/10.1007/BF01036704, 1984.

Wennberg, P. O., Roehl, C., Blavier, J. F., Wunch, D., Landeros, J. and Allen, N.: TCCON data from Jet Propulsion Laboratory, Pasadena, California, USA, Release GGG2014R0, TCCON data archive, CDIAC, https://doi.org/10.14291/tccon.ggg2014.jpl02.R0/1149297, 2014a.

Wennberg, P. O., Roehl, C., Wunch, D., Toon, G. C., Blavier, J. F., Washenfelder, R., Keppel-Aleks, G., Allen, N. and Ayers, J.: TCCON data from Park Falls, Wisconsin, USA, Release GGG2014R0, TCCON data archive, CDIAC, https://doi.org/10.14291/tccon.ggg2014.parkfalls01.R0/1149161, 2014b.

Wennberg, P. O., Wunch, D., Roehl, C., Blavier, J. F., Toon, G. C., Allen, N., Dowell, P., Teske, K., Martin, C. and Martin, J.: TCCON data from Lamont, Oklahoma, USA, Release GGG2014R0, TCCON data archive, CDIAC, https://doi.org/10.14291/tccon.ggg2014.lamont01.R0/1149159, 2014c.

Wunch, D., Wennberg, P. O., Toon, G. C., Connor, B. J., Fisher, B., Osterman, G. B., Frankenberg, C., Mandrake, L., O'Dell, C., Ahonen, P., Biraud, S. C., Castano, R., Cressie, N., Crisp, D., Deutscher, N. M., Eldering, A., Fisher, M. L., Griffith, D. W. T., Gunson, M., Heikkinen, P., Keppel-Aleks, G., Kyrö, E., Lindenmaier, R., Macatangay, R., Mendonca, J., Messerschmidt, J., Miller, C. E., Morino, I., Notholt, J., Oyafuso, F. A., Rettinger, M., Robinson, J., Roehl, C. M., Salawitch, R. J., Sherlock, V., Strong, K., Sussmann, R., Tanaka, T., Thompson, D. R., Uchino, O., Warneke, T., and Wofsy, S. C.: A method for evaluating bias in global measurements of CO_2 total columns from space, Atmos. Chem. Phys., 11, 12317-12337, https://doi.org/10.5194/acp-11-12317-2011, 2011.

Yokota, T., Oguma, H., Morino, I., and Inoue, G.: A nadir looking SWIR sensor to monitor CO_2 column density for Japanese GOSAT project, Proceedings of the twenty-fourth international symposium on space technology and science, Miyazaki: Japan Society for Aeronautical and Space Sciences and ISTS, 887-889, 2004.

Yoshida, Y., Kikuchi, N., Morino, I., Uchino, O., Oshchepkov, S., Bril, A., Saeki, T., Schutgens, N., Toon, G. C., Wunch, D., Roehl, C. M., Wennberg, P. O., Griffith, D. W. T., Deutscher, N. M., Warneke, T., Notholt, J., Robinson, J., Sherlock, V., Connor, B., Rettinger, M., Sussmann, R., Ahonen, P., Heikkinen, P., Kyrö, E., Mendonca, J., Strong, K., Hase, F., Dohe, S., and Yokota, T.: Improvement of the retrieval algorithm for GOSAT SWIR XCO_2 and XCH_4 and their validation using TCCON data, Atmos. Meas. Tech., 6, 1533-1547, https://doi.org/10.5194/amt-6-1533-2013, 2013.

Zeng, Z.-C., Lei, L., Strong, K., Jones, D. B. A., Guo, L., Liu, M., Deng, F., Deutscher, N. M., Dubey, M. K., Griffith, D. W. T., Hase, F., Henderson, B., Kivi, R., Lindenmaier, R., Morino, I., Notholt, J., Ohyama, H., Petri, C., Sussmann, R., Velazco, V. A., Wennberg, P. O., and Lin, H.: Global land mapping of satellite-observed CO_2 total columns using spatio-temporal geostatistics, Int. J. Digit. Earth, 1-31, https://doi.org/10.1080/17538947.2016.1156777, 2016.

Zhang, X. Y., Wang, Y. Q., Niu, T., Zhang, X. C., Gong, S. L., Zhang, Y. M., and Sun, J. Y.: Atmospheric aerosol compositions in China: spatial/temporal variability, chemical signature, regional haze distribution and comparisons with global aerosols, Atmos. Chem. Phys., 12, 779-799, https://doi.org/10.5194/acp-12-779-2012, 2012.